Agricultural Water Management 280 (2023) 108232

Contents lists available at ScienceDirect

Agricultural Water Management

journal homepage: www.elsevier.com/locate/agwat

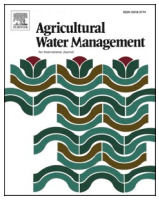

# Future trends of reference evapotranspiration in Sicily based on CORDEX data and Machine Learning algorithms

Fabio Di Nunno *, Francesco Granata

*University of Cassino and Southern Lazio, Department of Civil and Mechanical Engineering (DICEM), Via Di Biasio, 43, 03043 Cassino, Frosinone, Italy*

ARTICLE INFO

Handling Editor: Dr R Thompson

*Keywords:*
Climate change
Artificial Intelligence algorithms
Clustering
Ensemble models
Mediterranean climate
Irrigation planning

ABSTRACT

In years of increasing impact of climate change effects, a reliable characterization of the spatiotemporal evolutionary dynamics of evapotranspiration can enable a significant improvement in water resource management, especially as regards irrigation activities. Sicily, an insular region of Southern Italy, has exceptionally valuable agricultural production and high irrigation needs. In this study, the ETo reference evapotranspiration in Sicily was first evaluated on the basis of historical and future climate parameters, referring for future values to two climate scenarios characterized by different Representative Concentration Pathways: RCP 4.5 and RCP 8.5. Then, the Hierarchical algorithm was used to divide Sicily into three homogeneous regions, each characterized by specific ETo features. In addition, some Machine Learning (ML) algorithms were used to develop forecasting models based on only historical data. Support Vector Regression (SVR) was used to predict the future values of $T_{min}$ and $T_{max}$, while an ensemble model based on Multilayer Perceptron (MLP) and M5P Regression Tree was developed for the ETo forecasting. Predictions made with the ensemble MLP-M5P model were compared with the ETo computed for the RCP 4.5 and RCP 8.5 future climate scenarios. During the forecast period, from 2001 to 2091, evapotranspiration increases were observed for all three clusters. For cluster C1, along the coast, percentage increases of 7.52%, 14.64% and 10.78%, were computed for RCP 4.5, RCP 8.5, and MLP-M5P, respectively, while, for cluster C3, in the inland, percentage increases were higher and equal to 8.12%, 16.71%, and 14.98%, respectively. The ensemble MLP-M5P model led to intermediate trends between RCP 4.5 and RCP 8.5, showing a high correlation with the latter ($R^2$ between 0.93 and 0.98). The developed approach, based on both clustering and forecasting algorithms, provided a comprehensive analysis of the reference evapotranspiration, with the detection of the different homogeneous regions and, at the same time, the evaluation of the evapotranspiration trends, both in coastal and inland areas.

## 1. Introduction

Evapotranspiration is one of the main processes in the water cycle and its assessment plays an essential role in water resource management. However, given the complexity involved with direct measurement, the estimation of evapotranspiration is commonly based on meteorological data, which allows the estimation of the ETo reference evapotranspiration. The physical-based Penman-Monteith equation (Allen et al., 1998), which combines radiometric and aerodynamic parameters, is recommended by the United Nations Food and Agriculture Organization (FAO) for the ETo evaluation in different climates worldwide (Fan et al., 2016). However, climate change is affecting the hydrological cycle, and its effects will be probably more dangerous for arid and semi-arid climates, characterized by low rainfalls and high temperatures (Goyal and Gaur, 2022). Therefore, a spatio-temporal analysis of the future evapotranspiration trends may be crucial for predicting imbalances in regional hydrologic supply and enhancing water resources management (Yang et al., 2020).

The considerable variety of climates worldwide can lead to very different ETo trends depending on the local climatic features. Chaouche et al. (2010) investigated the spatio-temporal evolution of ETo for a Mediterranean climate area of France, showing increasing trends more marked close to the coast. Pandey and Khare (2018) and Prävälie et al. (2019) also detected an increasing ETo trend for the humid tropical climate of the Narmada River watershed, India, and for the temperate continental climate of Romania, respectively. Jerin et al. (2021) investigated the reference evapotranspiration trends for the tropical monsoon climate of Bangladesh, showing how, over the period 1980–2015,

* Corresponding author.
*E-mail addresses:* fabio.dinunno@unicas.it (F. Di Nunno), f.granata@unicas.it (F. Granata).

https://doi.org/10.1016/j.agwat.2023.108232
Received 25 July 2022; Received in revised form 8 February 2023; Accepted 11 February 2023

increasing and decreasing trends can be observed during the monsoon and dry periods, respectively. However, the authors highlighted a decreasing trend for the annual ETo. Different literature studies show a decreasing trend for semi-arid (She et al., 2017; Xu et al., 2018) and arid areas of China (Li et al., 2017). However, Fu et al. (2022) investigated the terrestrial evapotranspiration trends at China's land scale showing a significant linear increasing trend since 2000 for 87.03% of the study area, considering all agricultural regions of China.

Estimating ETo using the Penman-Monteith equation over large areas is often complicated by the lack of sufficiently widespread measurement stations for climate variables. This problem can be overcome by relying on the results of projects based on the combination of several Global Climate Models (GCMs) and Regional Climate Models (RCMs), which provide climatic variables in most regions of the world with different spatio-temporal resolutions and different climate scenarios. These allow an evaluation of present and future evapotranspiration even in poorly gauged areas. Examples of these projects are the Coordinated Regional Climate Downscaling Experiment (CORDEX, Gutowski et al., 2016) and Coupled Model Intercomparison Project (CMIP, Eyring et al., 2016).

In the last decades, ML-based models proved to be able to provide accurate predictions of hydrological variables, including evapotranspiration, with the advantage of a high computational speed without the need to define analytical relationships between exogenous variables (inputs) and targets (Di Nunno and Granata, 2020; Granata and Di Nunno, 2021a). Furthermore, in recent years, in order to improve the forecasting accuracy of ML algorithms, the research has been oriented toward the development of deep learning models (e.g., one-dimensional Convolutional Neural Network and Long Short-Term Memory network, Chia et al., 2022a, 2022b) and ensemble or hybrid models (Tikhamarine et al., 2019; Karbasi et al., 2022; Malik et al., 2022). However, investigations on future evapotranspiration trends through a comparison between the ETo evaluated on the basis of future data of the climatic variables and the ML approach are, to date, still very little debated. Yin et al. (2017) investigated the future variability of ETo using two ML Algorithms: Extreme Learning Machine (ELM) and SVR, in a mountainous inland watershed in north-west China. The authors considered eight GCMs from the CMIP5 under two RCP climate scenarios: RCP 4.5 and RCP 8.5. They showed how both ELM and SVR methods are characterized by good performance in estimating the ETo for the future period 2010–2099. Maqsood et al. (2022) investigated the response of ETo under three RCP climate scenarios: RCP 2.6, RCP 4.5, and RCP 8.5 using the second-generation Canadian Earth System Model (CanESM2). In particular, the authors estimated ETo for western, central, and eastern parts of Prince Edward Island (Canada) using the Hargreaves equation, with $T_{max}$ and $T_{min}$ for three future periods: 2011–2040, 2041–2070 and 2071–2100. Then, the authors employed three different artificial neural networks (ANNs) algorithms: One-Dimensional Convolutional Neural Network (1D-CNN), Long-Short Term Memory (LSTM), and MLP, for the ETo estimation, showing good accuracy. Kadkhodazadeh et al. (2022) analyzed the ETo trends for the period 2021–2050 at nine stations in the two basins of Lake Urmia and Sefidrood, Iran. In particular, the authors evaluated ETo by the Penman-Monteith equation, based on three different CMIP6 global climate models. Then, they carried out an ETo modeling implementing six ML algorithms: multiple linear regression (MLR), multiple non-linear regression (MNLR), multivariate adaptive regression splines (MARS), model tree M5 (M5), random forest (RF), and least-squares boost (LSBoost), with promising results.

A forecast model of the future ETo can be valid for a more or less large area, as long as the area is characterized by a certain homogeneity of the features affecting the ETo. Homogeneous evapotranspiration regions can be identified by means of clustering algorithms. Xing et al. (2016) applied the Rotated Empirical Orthogonal Function (REOF) clustering method to identify homogenous regions of ETo in China, based on the annual ETo times series from 602 stations for the period 1961–2011. Masanta and Vemavarapu (2020) detected eighteen homogeneous ETo regions in India using a fuzzy dynamic clustering approach, with climate variables as predictors. Chen et al. (2020) applied the K-means clustering algorithm for the ETo analysis in Northeast plain, China. The authors used the daily average values of maximum and minimum temperature, relative humidity, extraterrestrial radiation, and solar radiation, to group all weather stations with the clustering algorithm. Hobeichi et al. (2021) also applied the k-means algorithm on a global scale, with the detected clusters that included three wet and three dry regimes and provided an approximation of Köppen–Geiger climate classes.

The aim of this study is to provide a characterization of the ETo trends in Sicily, Southern Italy, based on a spatio-temporal analysis. A step-by-step description of the modeling procedure is provided in Section 2.7.

Sicily has exceptionally valuable agricultural production and also high irrigation requirements, in the context of scarcity of water resources. An accurate assessment of future trends in evapotranspiration is crucial to evaluate the impact of climate change on surface water availability in Mediterranean climate areas such as Sicily. Liuzzo et al. (2015) investigated the effect of climate change on water resource availability for a sub-basin of Belice catchment, Sicily, showing how the decreasing trends of precipitation involved a decrease in surface and groundwater resources, with the latter enhanced by the potential evapotranspiration changing. The authors also highlighted the impact on the reservoir management for Garcia Lake, Sicily, showing how in the future the reservoir will no longer be able to satisfy the water demands. This will lead to the need to reduce both agricultural water demand, through more efficient irrigation systems, and water leakages, which chronically affect water supply systems in southern Italy. Viola et al. (2016) also investigated the future evapotranspiration-runoff relationship (scenarios RCP 4.5 and RCP 8.5) for one of the largest Sicilian basins, the Imera Meridionale river basin, showing that future evapotranspiration changing will lead to a sharp reduction of the runoff as the reference evapotranspiration and temperature increase and the precipitation reduces. Varotsos et al. (2021) investigated the implication of climate change on the agricultural sector of three Mediterranean islands: Sicily, Crete and Cyprus, based on the EURO-CORDEX data and the two scenarios RCP 4.5 and RCP 8.5. Authors showed marked changing in the average, maximum, and minimum temperatures during the period 2031 and 2060 with, however, a less pronounced reduction of the total precipitation. The authors highlighted the impact of these variations on the main crops cultivated in the three islands. In particular, the expected warming mostly in spring and summer might expose the crops to an adverse impact on the plants' phenological stages, affecting both production and quality. For example, for the olive tree, widespread in large areas of Sicily, the temperature increases can lead to positive effects on trunk and fruit growth. However, climate change can bring also negative impacts on flowering bud differentiation, which requires an appropriate low-temperature period, and the increase of olive fly infestations, reducing final yield and quality.

Moreover, future climate projections represent extreme conditions corresponding to assumed emission scenarios but conditioned by future environmental policies and certainly affected by significant uncertainty. Further considerable uncertainty is due to the complexity of global and regional models (Yin et al., 2017). In this scenario, the ML-based models, which are relatively simple to develop on the basis of historical data alone, can provide reliable alternative forecasting tools, which are also useful for validating the results of the more complex GCMs and RCMs or highlighting their discrepancies.

A study of the spatio-temporal evolution of regional reference evapotranspiration over the long term, based on clustering and ML algorithms, with subsequent comparison of the results with extreme climate scenarios, is certainly novel compared to the current literature. The issue takes on even greater importance for the area investigated in this study, Sicily, where climate change can significantly increase the risk of desertification. In this context, the clustering results, in addition

to allowing the recognition of homogeneous ETo areas, were analyzed in context with the agricultural land use to correlate the reference evapotranspiration with the different crop water demands, allowing the identification of the most sensitive areas in terms of potential future water deficit. From this point of view, reliable future ETo forecasting is crucial. Although the MLP algorithm has recently been applied by Maqsood et al. (2022) to investigate the ETo trends under different future climate scenarios, the ensemble model based on MLP and M5P algorithms for the ETo prediction, besides being a further element of novelty, aimed at significantly improving the performance of individual algorithms, which are not always able to provide satisfactory predictions, especially for long-term forecast horizons.

Therefore, this study aims to overcome the limitations of the existing literature on the reference evapotranspiration prediction in Sicily, proposing a combined clustering-forecasting approach that can provide useful information for the present and future management of water resources for different purposes.

## 2. Materials and methods

### 2.1. Study area

Sicily is the largest island in the Mediterranean Sea and has a typical Mediterranean climate, with hot, dry summers and mild, wet winters. Moreover, especially along the southwestern coast, the African anticyclone brings frequent and marked temperature increases (Benedetto and Giordano, 2008, Fig. 1a).

During the winter, the average temperature varies from 4 °C in the inland province of Enna to 9.7 °C and 11.5 °C on the west coast of Trapani and the northeast coast of Messina, respectively. During the summer, the average temperature varies from about 28 °C inland to about 30° along the coast. Rainfall is higher along the east coast, with 709 mm of annual precipitation in 109 rainy days for Messina, compared to the west coast, with 446 mm of annual precipitation in 88 rainy days in Trapani. In addition, inland areas showed lower annual precipitation than the coast, with 358 mm of annual precipitation on 69 rainy days for the city of Enna. However, annual rainfall is far below the national average.

One of the main economic activities of the region is agriculture, with more than 1,600,000 ha of agricultural land, corresponding to about 64% of Sicily's total surface. Fig. 1b provides the agricultural land cover of Sicily, based on CORINE (Coordination of information on the environment) Land Cover data for the year 2018, with the 3-level nomenclature. Fruit trees, which cover 11% of agricultural land, are mostly concentrated along the east coast and particularly in the province of Catania. Vineyards and olive groves, which cover 9% and 12% of agricultural land, respectively, are more widespread along the west coast. Permanently irrigated lands, which include greenhouses, cover only 4% of the agricultural land and are more widespread in the southeastern part of the island. In addition, 48% of agricultural land is represented by

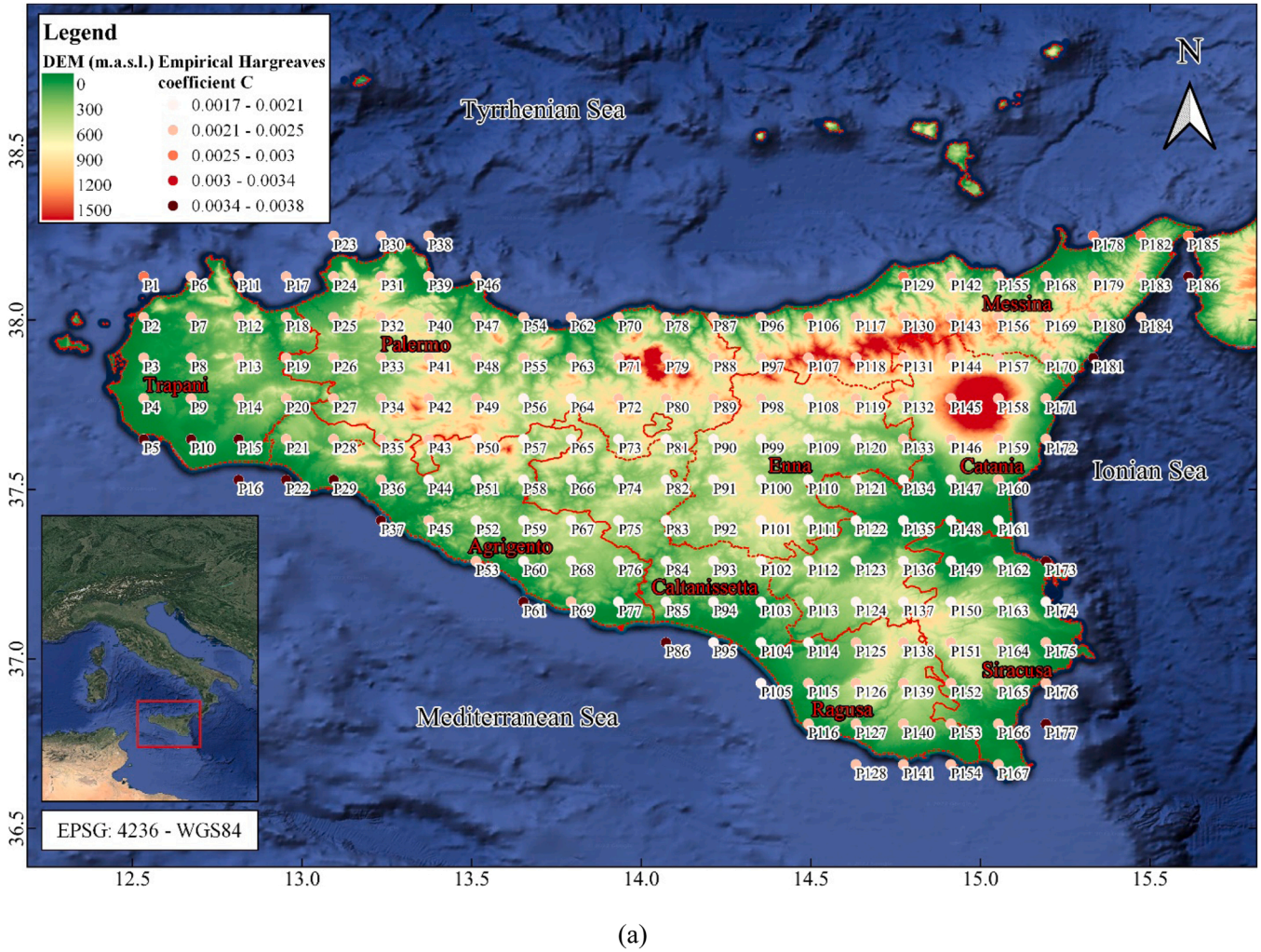


(a)

**Fig. 1.** Location of the gridded data points in Sicily with: a Digital Elevation Model (DEM) representation, the Empirical Hargreaves coefficient distribution, and an indication of the Sicilian Province (a); Agricultural land cover of Sicily (b).

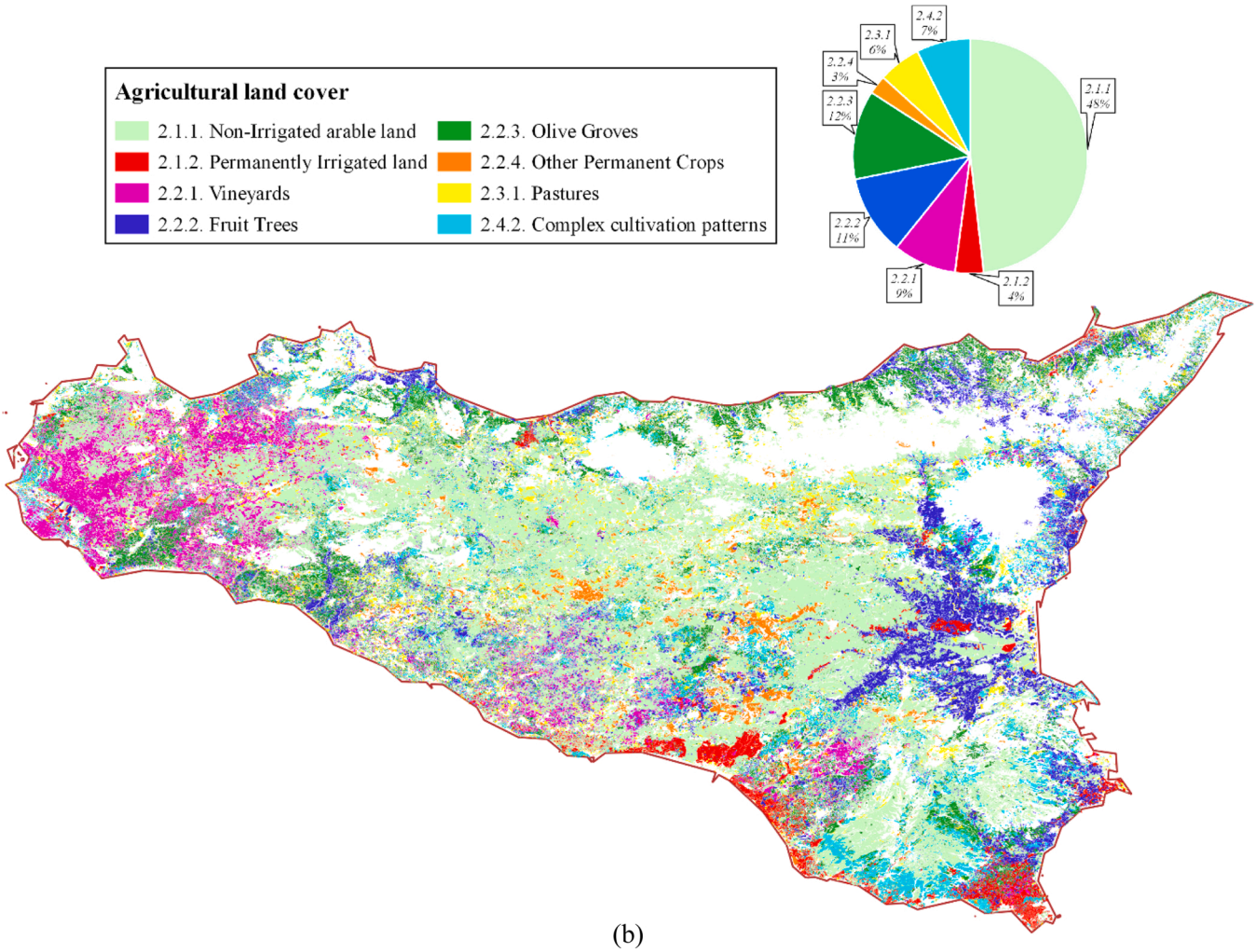


(b)

**Fig. 1.** (*continued*).

non-irrigated arable land, which includes rainfed and sporadically irrigated land with non-permanent devices.

In addition to agricultural land use, the factor that plays a key role in the management of water resources is the irrigation requirements of each crop. These also vary considerably from area to area in Sicily depending on the climatic and pedological conditions. Vineyards require from 1200 to 1800 $m^3$/ha • year, going from the provinces of Caltanissetta and Ragusa (south-east) to the province of Palermo (north-west), respectively. Great variability is also observed for olive groves, which require from about 1200 $m^3$/ha • year for the provinces of Caltanissetta, Ragusa, and the northern portion of Trapani (west), to about 2000 $m^3$/ha • year for the provinces of Catania, Palermo, and the southern portion of Trapani. Fruits trees require about 3500 $m^3$/ha • year for the whole region, with the only exception of the Catania province where the greatest presence of orchards is observed, for which 3800 $m^3$/ha • year are indicated (Regione Sicilia, 2010).

However, it should be seriously considered that the impacts of climate change on the hydrological cycle have been observed in recent years, related to rising average temperatures and evapotranspiration rates, leading to a significant increase in irrigation demands (Viola et al., 2014). This, together with the reduced availability of surface water and groundwater, is related to the negative rainfall trend, which leads to an increased risk of desertification on the island (Liuzzo et al., 2015).

### 2.2. Dataset

Minimum ($T_{min}$) and Maximum ($T_{max}$) temperature grid data from the CORDEX project were used in this study. The CORDEX platform was developed by the World Climate Research Program (WCRP) with the aim of providing high-resolution climate datasets in several locations around the world (Gutowski et al., 2016). Specifically, the CORDEX experiments consist of simulations representing different future socio-economic scenarios based on different combinations of RCMs and GCMs.

The GCM model used was the MOHC-HadGEM2-ES, developed by the Met Office Hadley Centre (MOHC) with the HadGEM2 family of configurations, including the Earth-System (ES) components like dynamic vegetation, ocean biology, and atmospheric chemistry. The HadGEM2 physical model includes improvements designed to address specific systematic errors found in the previous climate configuration, HadGEM1, related to continental temperature biases of the northern hemisphere and tropical sea surface (The HadGEM2 Development Team, 2011). The RCM model was the CLMCom-CCLM4–8–17 for the European domain (EUR-11, CLMCom, 2017). Since climate features, like temperature and rainfall, are highly spatially variable due to the rather complex orography of Sicily (Forestieri et al., 2018a; Peres et al., 2020), the bias correction included in the GCM model allowed to reduce the errors between the observed and simulated hydrological data based on CORDEX climate models, as demonstrated in several literature studies in other Mediterranean areas (Piani et al., 2010; Dosio, 2016). Forestieri

et al. (2018b) demonstrated the capability of CORDEX models to reproduce extreme rainfall measured at different stations in Sicily. Peres et al. (2020) also investigated the skill of several EURO-CORDEX RCMs, with grid-size of 0.11°, in reproducing the seasonal temperature and precipitation regime for Calabria and Sicily, showing higher performances for temperature (which is the variable considered in the present study) with respect to precipitation. Moreover, the combination of the two climate models, regional and global, has recently led to an accurate analysis of climate change in eastern Greece and in particular on the island of Crete, which has a climate similar to that of Sicily (Markantonis et al., 2022).

Two extreme RCP scenarios, RCP 4.5 and RCP 8.5, were considered as climate projections. RCPs are greenhouse gas concentration trajectories adopted by the Intergovernmental Panel on Climate Change (IPCC). RCP 4.5 is an intermediate scenario with emissions peaking around 2040 and declining until 2100. RCP 4.5 can be regarded as the most likely scenario, as it considers the exhaustible nature of non-renewable fuels (Höök et al., 2010). RCP 8.5 represents the worst-case climate change scenario, as it considers an increase in emissions throughout the 21st century.

The spatial resolution of the dataset grid was equal to 0.11°, with 186 gridded data points covering the entire island (Fig. 1a). The dataset spans from 1951 to 2005 for historical data, and from 2006 to 2100 for the RCP scenarios, with a monthly time scale. In addition to $T_{min}$ and $T_{max}$, the extraterrestrial radiation ($R_a$) was computed for each gridded data point, from 1951 to 2100, expressed as:

$$R_a = \frac{24 \bullet 60}{\pi} G_{sc} d_r [(\omega_s \sin\varphi \sin\delta) + (\cos\varphi \cos\delta \sin\omega_s)] \quad (1)$$

where $G_{sc}$ is the solar constant, $d_r$ is the inverse relative distance Earth-Sun, $\omega_s$ is the sunset hour angle, φ is the latitude and δ is the solar declination (Zotarelli et al., 2013).

### 2.3. Reference evapotranspiration

In order to calculate the monthly average daily reference evapotranspiration (ETo), the Hargreaves-Samani (HE) equation was used (Hargreaves and Samani, 1985), expressed as:

$$ET_0 = C \bullet R_a \left( \frac{T_{max} + T_{min}}{2} + 17.8 \right) \sqrt{T_{max} - T_{min}} \quad (2)$$

where C is the empirical Hargreaves coefficient. The main advantage of this equation, compared to the more complex Penman-Monteith model, is that it only requires extraterrestrial radiation and the time series of the minimum and maximum temperature (Di Nunno and Granata, 2020; Elbeltagi et al., 2020). However, the accuracy in the estimation of ETo depends on the value of the empirical coefficient C, which can vary significantly depending on the morphoclimatic characteristics of the study area. Mendicino and Senatore (2013) proposed a regionalization of the Hargreaves coefficient, with different equations for each subregion of Southern Italy. The authors showed how a properly calibrated HS equation provides better performances than the original HS. Furthermore, in comparison to the well-known FAO Penman-Monteith equation, which however requires several parameters for the ETo calculation, the calibrated HS equation led to very close ETo estimation for many locations in Southern Italy (including about 40 measurement stations located throughout Sicily). For the evaluation of the empirical Hargreaves coefficient C in Sicily, Mendicino and Senatore (2013) proposed the following equation:

$$C = 1 \bullet 10^{-5} \overline{\Delta T^2} - 0.0004 \overline{\Delta T} + 0.0049 \quad (3)$$

where $\overline{\Delta T}$ is the average value, computed for each data point, of the difference between $T_{max}$ and $T_{min}$. In particular, the calculated value of C for the 186 gridded points ranged from 0.0017 and 0.0038, with the higher values along the coast, in particular in the south of the region, and the lowest values in the south-eastern inland (see Fig. 1a).

Therefore, the calibrated HS equation was used to evaluate both the historical ETo, from 1951 to 2005, and the future ETo for the RCP 4.5 and RCP 8.5 climate scenarios, from 2006 to 2100, considering the individually calculated values of both C and $R_a$ for each grid point.

### 2.4. Clustering procedure

Clustering can be defined as a classification process of a large dataset into a smaller number of groups. Therefore, data belonging to the same cluster have common characteristics while data belonging to different clusters are characterized by some heterogeneity (Barton et al., 2016). Recently, the Hierarchical clustering algorithm has found application for various hydrological analyses (Aladaileh et al., 2019; Xulu et al., 2019; Neto et al., 2021). The advantages of hierarchical clustering compared to other algorithms, such as k-means, are that the number of clusters does not have to be determined prior to clustering and that the process can be evaluated with the aid of a dendrogram chart, which can be used to better understand the overall picture in which the data are clustered (Berhanu et al., 2015).

The hierarchical clustering algorithm was used to divide the study area into homogeneous areas. Several statistical parameters of the time series of ETo were preliminary considered as inputs for the clustering procedure: the minimum, mean, and maximum values of the ETo ($ETo_{Min}$, $ETo_{Mean}$, $ETo_{Max}$, respectively), the ETo standard deviation, mode, and skewness ($ETo_{std}$, $Eto_{mode}$, and $ETo_{skew}$, respectively), the number of months with ETo between 0 and 1.5 mm/day ($ETo_{0–1.5}$), 1.5 mm/day and 3 mm/day ($ETo_{1.5–3.0}$), 3 mm/day and 4.5 mm/day ($ETo_{3.0–4.5}$), 4.5 mm/day and 6 mm/day ($ETo_{4.5–6.0}$). All these parameters were computed on the historical data, to also take into account the frequency with which higher or lower values of evapotranspiration were observed.

However, clustering can be adversely affected by the high dimensionality of the dataset (Dash and Koot, 2009). Furthermore, the optimal number of clusters is also not known a priori. Therefore, in order to identify both the input parameters that have the greatest influence on the clustering and the optimal number of clusters, a preliminary analysis based on the Silhouette technique was performed. Silhouette is a well-known technique for the interpretation and validation of coherence in clustering applications, which provides a measure of how similar an object is to its cluster compared to other clusters (Rousseeuw, 1987; Shutaywi and Kachouie, 2021). The silhouette score ranges from − 1, which indicates that the clusters are incorrectly assigned, to 1, which indicates that clusters are well-distinguished from each other. Score values close to 0 indicate that the distance between clusters is not significant.

The clustering process starts by considering each observation as a separate cluster. Then, it follows an iterative process based on two main steps: (i) the detection of a couple of clusters that are closest and (ii) the merge of two clusters based on a linkage criterion. The process stops when all the clusters are merged. The distance between two clusters has been evaluated through the Manhattan distance, expressed as:

$$J(X;V) = \sum_{i=1}^{c} \sum_{ki} \left| x_k^{(i)} - v_i \right| \quad (4)$$

where $V = \{v_i \mid i = 1, \ldots, c\}$ are the centers of the $c$ clusters, $x_k^{(i)}$ is the $k^{th}$ data point belonging to the $i^{th}$ cluster, and $x_k^{(i)} - v_i$ is the distance between each data point and his cluster center $v_i$, with $v_i$ computed as:

$$v_i = \frac{\sum_{k=1}^{N_i} x_k}{N_i}, x_k \in A_i \quad (5)$$

where $A_i$ represents the set of $N_i$ points related to the $i^{th}$ cluster.

Therefore, the Manhattan distance evaluates the distance between two points by aggregating the absolute difference in pairs between each variable (Callahan and Bridge, 2021).

Conversely, other distance formulations, such as the Euclidean distance, aggregate the squared difference between each variable. This means that, if two data points are similar for most variables but different for one of them, the evaluation using Euclidean distance will be overly influenced by that single difference. In contrast, the Manhattan distance will be more influenced by the similarity of the other variables, being more robust and less affected by outliers.

To evaluate the distance between clusters, the Ward linkage was considered, which evaluates the distance between the two clusters as the increase in the sum of squares error (SSE) after merging two clusters into a single one, expressed as:

$$D(r,s) = SSE_{rs} - (SSE_r - SSE_s) \tag{6}$$

where $D(r,s)$ is the distance between the clusters $r$ and $s$. The performance of the Ward linkage where preliminary compared with other linkages: single, complete and average. In particular, the Ward linkage led to the most robust results, with the identification of clusters consistent with the climatic and morphological features of Sicily. Single, complete and average linkage led to anomalous small clusters that are not consistent with the characteristics of the island. Therefore, the results of Hierarchical clustering (described in Section 3.1) were obtained considering the Manhattan distance combined with the Ward linkage.

### 2.5. Machine Learning forecasting algorithms

Some ML algorithms were used to develop forecasting models. Support Vector Regression (SVR) was used for predicting $T_{min}$ and $T_{max}$ in the future period 2006–2100, after using historical CORDEX data of the same variables from 1951 to 2005 for training.

Subsequently, an ensemble model based on MLP and M5P was employed for the prediction of ETo in the period 2006–2100. The Bayesian Optimization (BO) process was used for the selection of the input parameters and ML hyperparameters, and for the evaluation of the optimal number of lagged values (Wu et al., 2019). The use of optimization algorithms is widely spread in hydrological applications to improve the performance of ML algorithms (Di Nunno et al., 2022).

In particular, the parameters initially considered for the prediction were: $R_a$, $T_{min}$, and $T_{max}$. The BO algorithm led to a reduction of the number of parameters, including only $R_a$ and $T_{min}$. However, a preliminary analysis was also performed to assess the impact of $T_{max}$ as a further input variable for the ETo modeling. This analysis showed an anomalous increase in the minimum peaks of ETo, inconsistent with both historical data and future scenarios RCP 4.5 and RCP 8.5.

#### 2.5.1. Support Vector Regression (SVR)

Support Vector Machine algorithms (SVMs) are supervised ML models used for both classification and regression problems (Cortes and Vapnik, 1995; Vapnik, 1998; Pham et al., 2022). In the latter case, it is generally indicated as Support Vector Regression (SVR). SVR has been widely applied in the prediction of hydrological variables, including evapotranspiration, allowing the implementation of individual or hybrid models with other ML and optimization algorithms (Yin et al., 2017; Tikhamarine et al., 2020a, 2020b; Chia et al., 2022a, 2022b). Moreover, SVR was also successfully applied for long-term temperature forecasting (Aghelpour et al., 2019), in agreement with its use in the present study.

SVR algorithm aims to find a function $f(x)$ with a deviation lower than a given $\varepsilon$ value from the target $y_i$. Based on the training dataset: $\{(x_i, y_i), i = 1, \ldots, l\} \subset X \times R$, where X is the input space, it is necessary to solve a constrained convex optimization problem by minimizing the Euclidean norm $||w||^2$. Given a function $f(x) = \langle w, x\rangle + b$, with $b \in R$ and $w \in X$, the optimization problem can be expressed as:

$$\text{minimize}: \frac{1}{2}\|w\|^2 + C_{SVR}\sum_{i=1}^{l}\left(\xi_i + \xi_i^*\right) \tag{7}$$

$$\text{subject to}: \begin{matrix} y_i - \langle w, x_i\rangle - b \le \varepsilon + \xi_i \\ \langle w, x_i\rangle + b - y_i \le \varepsilon + \xi_i^* \end{matrix} \tag{8}$$

with both deviation and function flatness depending on the constant $C_{SVR} > 0$. In addition, since often a significant error must be tolerated, the slack variables $\xi_i$, $\xi_i^*$ were introduced in the constraints. The SVR effectiveness mainly depends on the kernel function selection. The polynomial kernel was considered in this study, which can be expressed as:

$$k(x_i, x_j) = \left(1 + x_i \bullet x_j\right)^d \tag{9}$$

where $d$ is the degree of the polynomial kernel. BO process allowed to find the values of the constant $C_{SVR}$ and of the degree $d$, that led to the best predictions: $C_{SVR} = 1.8$; $d = 1.03$. In addition, the optimal lagged value of the input variables for the prediction was equal to 120 months.

#### 2.5.2. Multilayer Perceptron (MLP)

Multilayer Perceptron (MLP) is a feedforward ANN (Rosenblatt, 1961; Murtagh, 1991) with three types of layers: input, hidden, and output. The input layer consists of a set of nodes corresponding to the input features. One or more hidden layers contain neurons that process the values of the input layer based on a weighted linear sum followed by a non-linear activation function. Then, the output layer gets the outcomes from the last hidden layer, providing the predicted values. Backpropagation learning algorithm was used for the MLP neurons training. In addition, the network optimal structure for the present study includes one hidden layer, with a neuron number that was equal to (number of input variables + 1)/2, with the Sigmoid activation function. The optimal learning and momentum rates of the backpropagation algorithm were 0.3 and 0.2, respectively.

#### 2.5.3. M5P

The M5P algorithm develops prediction models based on decision trees with real numbers as target variables, usually referred to as regression trees (Quinlan, 1992). Three types of nodes are included in a regression tree: the root node, which include the complete dataset, the internal nodes, which define the conditions on the input variables, and the leaf nodes, consisting of linear regression models of the target values. M5P is based on an iterative process that divides the input dataset into subsets, on which the linear regression models are built. The division is performed by searching the subsets couples that lead to a maximization of the least-squared deviation (LSD) function, with:

$$R(t) = \frac{1}{N(t_n)}\sum_{i\in t}(y_i - y_m(t_n)) \tag{10}$$

where $R(t_n)$ is the $t_n$ node within variance, $N$ is the subset units' number, $y_i$ is the $i^{th}$ target variable value, and $y_m$ is the target variable mean. The function $\Phi(s_p, t_n)$ to be maximized is expressed as:

$$\varnothing\left(s_p, t_n\right) = R(t_n) - p_L R(t_L) - p_R R(t_R) \tag{11}$$

with $p_L$ and $p_R$ that represent the portion units allocated to the left node $t_L$ and right node $t_R$, respectively, and $s_p$ that indicate the split value (Granata and Di Nunno, 2021b). In addition, the pruning technique is employed for the fully developed tree, removing branches with a low contribution to the prediction ability. This technique made it possible to reduce the tree size and avoid overfitting problems. The optimization process showed that the number of instances in a leaf node to get the best predictions was 4.

#### 2.5.4. Ensemble model MLP-M5P

In order to improve the prediction ability of the individual ML

models, the Stacking ML technique was used to build an ensemble model based on both MLP and M5P algorithms. Stacking combines multiple regression or classification models by means of a meta-classifier (Li et al., 2020), which was, for the present study, the Elastic Net algorithm (Zou and Hastie, 2005). In particular, the models based on the individual ML algorithms were first developed on the training dataset, then, based on the outcomes of each individual model, the Elastic Net was employed to develop the ensemble model. It should be noted that the parameters considered for the individual MLP and M5P algorithms, were the same reported in Sections 2.5.2 and 2.5.3. In addition, the number of lagged values of input variables ($R_a$, $T_{min}$, and $T_{max}$) and of ETo was assessed based on the BO process, finding an optimal value of 12 months for both inputs and target. This means that to make a prediction at time *t*, the values of both input and target parameters from *t-12* to *t-1* were taken into account.

### 2.6. Evaluation metrics

In this study, five different evaluation metrics were used, not following the standard approach of comparing predicted and experimental values of a given quantity, but comparing the ETo predictions obtained from the MLP-M5P hybrid model with those obtainable from the climate variables provided by the RCP 4.5 and RCP 8.5 future scenarios. Specifically, the metrics are the Coefficient of determination ($R^2$), which provides an evaluation of the linear correlation between the predictions of two models, the Root Mean Square Error (RMSE), which provides the root of the total squared difference between the predictions of two models normalized by the number of samples, the Mean Absolute Error (MAE), equal to the absolute difference between the predictions of two models normalized by the number of samples, the Mean Absolute Percentage Error (MAPE), equal to the relative difference between the predictions of two models normalized by the number of samples, and the Mean Directional Accuracy (MDA), that compares the forecast direction (upward or downward) of two models, providing the probability that they follow the same direction. Evaluation metrics can be expressed as:

$$R^2 = 1 - \frac{\sum_{i=1}^{n} \left(f_1^t - f_2^t\right)^2}{\sum_{i=1}^{n} \left(\overline{f_2} - f_2^t\right)^2} \tag{12}$$

$$RMSE = \sqrt{\frac{\sum_{i=1}^{n} \left(f_1^t - f_2^t\right)^2}{n}} \tag{13}$$

$$MAE = \frac{\sum_{i=1}^{n} \left|f_1^t - f_2^t\right|}{n} \tag{14}$$

$$MAPE = \frac{\sum_{i=1}^{n} \left|\frac{f_1^t - f_2^t}{f_2^t}\right|}{n} \tag{15}$$

$$MDA = \frac{\sum_{i=1}^{n} \mathbf{1}\mathrm{sgn}\left(f_1^t - f_1^{t-1}\right) = \mathrm{sgn}\left(f_2^t - f_2^{t-1}\right)}{n} \tag{16}$$

where $f_1^t$ and $f_2^t$ are the predicted values of the first and second models at time *t*, $f_1^{t-1}$ and $f_2^{t-1}$ are the predicted values of the first and second models at time *t-1*, $\overline{f_2}$ is the averaged value of the prediction for the second model, and n is the total amount of forecasting data in the time series.

### 2.7. Modeling procedure

The modeling procedure (Fig. 2) consists of the following steps:

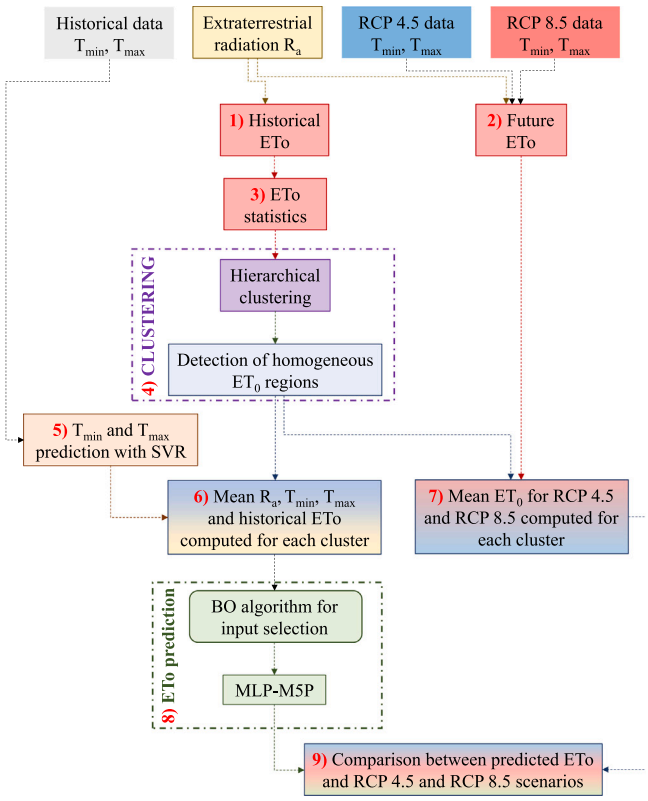


**Fig. 2.** Flowchart of the modeling procedure.

1. Starting from the historical time series of $R_a$, $T_{min}$, and $T_{max}$ (1951–2005), the calibrated HS (Eq. 2) was used to calculate ETo;
2. Based on the values of $T_{min}$ and $T_{max}$ for the future scenarios RCP 4.5 and RCP 8.5 (2006–2100) and on $R_a$, the HS equation (Eq. 2) was used to calculate the future values of ETo;
3. The statistical parameters of interest of the ETo historical time series (1951–2005) were calculated for each data point;
4. Based on the parameters assessed at Point 3, the homogenous ETo regions were detected by means of Hierarchical clustering;
5. Future values of $T_{min}$ and $T_{max}$ were predicted by means of the SVR algorithm. In particular, the forecasting models were trained considering only the historical data (1951–2005) of $T_{min}$ and $T_{max}$, respectively, and used for predictions in the future period (2006–2100);
6. The mean values of $R_a$, $T_{min}$, $T_{max}$, and historical ETo (Point 1) were calculated for each detected cluster (Point 4), including both historical data and prediction performed with the SVR algorithm for $T_{min}$ and $T_{max}$ (Point 5);
7. The mean value of ETo for the future scenarios RCP 4.5 and RCP 8.5 (Point 5) were calculated for each cluster (Point 4);
8. Prediction of ETo based on the ensemble MLP-M5P model, with the mean value of $R_a$, $T_{min}$ and $T_{max}$ and historical ETo (Point 6) as input parameters and the BO algorithm for the input selection;
9. Comparison, for each cluster (Point 4), of the ETo predicted by means of the ensemble MLP-M5P model (Point 8) with the ETo of the future scenarios RCP 4.5 and RCP 8.5 (Point 7).

The proposed approach provided a spatio-temporal characterization of ETo based on the detection of homogeneous regions and the prediction of the future ETo, with a comparison with different climate scenarios.

## 3. Results

### 3.1. Clustering

The optimization of the number of clusters and of the proper subset of input variables was performed based on the Silhouette technique (see Section 2.4). As shown in Table 1, the best mean Silhouette score, equal to 0.412, was obtained for a number of clusters equal to 3 and assuming seven input variables: $ETo_{Min}$ $ETo_{Mean}$ $ETo_{Max}$, $ETo_{0–1.5}$, $ETo_{1.5–3.0}$, $ETo_{3.0–4.5}$, $ETo_{4.5–6.0}$. In addition, Table 2 reports the mean values of ETo statistics for the three clusters. Fig. 3 provides the Silhouette scores for all data points related to the three clusters. In addition, Fig. 4 provides a representation of the ETo clustering of Sicily obtained using the Inverse Distance Weighting (IDW) method as a spatial interpolation technique (Topçu et al., 2022), with the dendrogram diagram obtained from the Hierarchical clustering.

Cluster C1 includes mainly the eastern, western, and southern coastal areas, showing silhouette peaks of about 0.6 for the data points P182 and P185 located in the north-east of the island near the Strait of Messina, P1 in the north-west close to Trapani, and P37 in the south-west at the Platani river mouth nature reserve in Agrigento province. In contrast, the data points that show the lowest Silhouette, close to 0.01, are generally located on the border with cluster C2, showing a lower degree of belonging to cluster C1. In particular, P105 is located in the southeast at "Marina di Acate" (Ragusa province), while P38 is located at Capo Gallo Natural Reserve (Palermo province), surrounded by points belonging to cluster C2.

Cluster C2 includes the coastal portion of the island to the north, on the Tyrrhenian Sea, as well as the inland to the southeast and northwest. The highest Silhouette scores, of about 0.58, were computed for data points P18 and P19, along the coast and inland of the Gulf of Castellammare in the north-west (Trapani province), and for P150 in the inland of the Syracuse province in the south-east. The lower Silhouette score, close to 0.01 was computed for data point P122, in the inland of Catania Province in the east of the island, surrounded by points belonging to cluster C3.

Cluster C3 mainly covers the inland of Sicily in its central and eastern parts. Overall, the highest Silhouette score was computed for C3, with values of about 0.63 for data points P57, P81, and P73, located in the inland Agrigento and Caltanissetta provinces. The lower Silhouette score, close to 0.1, was instead computed for P68, located in the south of the island, close to the coast, and surrounded by both clusters C1 and C2.

**Table 1**
Mean Silhouette scores for different number of clusters and subsets of input variables (in bold the best value).

| Input variables | Number of Clusters | | | | | | |
|---|---|---|---|---|---|---|---|
| | 2 | 3 | 4 | 5 | 6 | 7 | 8 |
| $ETo_{Min}$, $ETo_{Mean}$, $ETo_{Max}$, $ETo_{std}$, $ETo_{mode}$, $ETo_{skew}$, $ETo_{0–1.5}$, $ETo_{1.5–3.0}$, $ETo_{3.0–4.5}$, $ETo_{4.5–6.0}$ | 0.403 | 0.385 | 0.294 | 0.32 | 0.291 | 0.262 | 0.284 |
| $ETo_{Min}$, $ETo_{Mean}$, $ETo_{Max}$, $ETo_{0–1.5}$, $ETo_{1.5–3.0}$, $ETo_{3.0–4.5}$, $ETo_{4.5–6.0}$ | 0.401 | **0.412** | 0.361 | 0.379 | 0.383 | 0.334 | 0.348 |
| $ETo_{Min}$, $ETo_{Mean}$, $ETo_{Max}$ | 0.406 | 0.389 | 0.289 | 0.319 | 0.293 | 0.274 | 0.295 |

Overall, cluster C1, covering mainly the coasts of Sicily, showed higher values of $ETo_{Min}$, $ETo_{Mean}$, and $ETo_{Max}$ compared to clusters C2 and C3, with also a higher frequency of months with intermediate ETo, between 1.5 and 3.0 mm/day ($ETo_{1.5–3.0}$), between 3.0 and 4.5 mm/day ($ETo_{3.0–4.5}$) and greater than 4.5 mm/day ($ETo_{4.5–6.0}$). In addition, C1 showed higher skewness ($ETo_{skew}$), indicating a greater positive asymmetry compared to the other clusters. Otherwise, cluster C3, which covers inland Sicily, showed lower values of $ETo_{Min}$ $ETo_{Mean}$ and $ETo_{Max}$ with a higher frequency of months with a low ETo between 0 and 1.5 mm ($ETo_{0–1.5}$). Cluster C2 showed intermediate values of the ETo statistics, compared to C1 and C3 with, however, the lower $ETo_{skew}$, indicating a more symmetric ETo distribution compared to C1 and C3, and the lower number of an intermediate ETo range between 1.5 and 3.0 mm/day ($ETo_{1.5–3.0}$).

It should also be noted that, although no geomorphological variables have been introduced in the clustering, the ETo statistics implicitly take them into account. For example, Cluster C3, which is representative of the inland, extends as far as the sea both to the north-west, with the Madonie and Nebrodi mountain ranges (elevation up to 1800 m.a.s.l., see Fig. 1a), and to the west, with the volcano Etna (elevation up to 3300 m.a.s.l.). This indicates how the clusters consider not only the distance from the sea but also the morphology of the territory.

Overall, the cluster analysis provided important insights into the heterogeneity of ETo, both in terms of magnitude and variation, across Sicily. At the same time, clustering has led to the identification of subregions with well-defined ETo characteristics within Sicily, which can be useful for the analysis of future ETo trends on larger scales, as well as providing useful hydrological and agronomic information for non-instrumented areas.

The agricultural land use for the three clusters was also assessed (Fig. 5). Cluster C1 showed the highest percentage of permanently irrigated land (2.1.2), accounting for 6% of the cluster surface. This type of land cover usually entails a high irrigation requirement, as it includes: irrigated arable crops, which require approximately 3600 $m^3$/ha • year in Sicily, horticultural crops, between 4000 and 6000 $m^3$/ha • year, and greenhouse crops, which are particularly widespread along the coasts for the production of vegetables, which have the highest irrigation requirement of 12000 $m^3$/ha • year. C1 showed also a higher percentage of vineyards (20%, 2.2.1) and olive groves (18%, 2.2.3), which involve irrigation demand between 1200 and 2000 $m^3$/ha • year (see also Section 2.1). Cluster C2 showed instead a higher percentage of fruit trees (16%, 2.2.2) and a slightly lower percentage of olive groves (17%, 2.2.3), compared to cluster C1. Fruit trees had higher water demands compared to vineyards and olive groves, with values between 3500 and 3800 $m^3$/ha • year. Cluster C3 showed a higher percentage of agricultural land with low water demands, non-irrigated arable land (50%, 2.2.1), other permanent crops (6%, 2.2.4), which are mainly represented by the eucalyptus trees typical of the Sicilian inland, and pastures (8%, 2.3.1).

Overall, although clusters C2 and C3 have larger agricultural surfaces, cluster C1 includes the agricultural land showed a greater concentration of agricultural land with higher water demand. Considering that C1 is also the cluster that showed the higher values of $ETo_{Min}$, $ETo_{Mean}$, and $ETo_{Max}$ compared to C2 and C3, the risk of a water deficit for the coastal areas of Sicily could become increasingly marked in the future.

### 3.2. ETo analysis for the different clusters

The ETo mean value predictions performed using the MLP-M5P ensemble model for each cluster were compared to the ETo values estimated for the RCP 4.5 and RCP 8.5 future scenarios. Cluster C1 showed a historical peak of 5.95 mm/day (Fig. 6a), with a 10-year average ETo showing very little change from 1951 to 1991, rising from 2.99 mm/day to 3.02 mm/day, with a lower peak in 1961 of 2.94 mm/day (Fig. 6c). Over the forecast period (Fig. 6b), a significant

**Table 2**
Mean values of ETo statistics, in mm/day, for the different clusters.

| Cluster | $ETo_{Min}$ | $ETo_{Mean}$ | $ETo_{Max}$ | $ETo_{std}$ | $ETo_{mode}$ | $ETo_{skew}$ | $ETo_{0–1.5}$ | $ETo_{1.5–3.0}$ | $ETo_{3.0–4.5}$ | $ETo_{4.5–6.0}$ |
|---|---|---|---|---|---|---|---|---|---|---|
| C1 | 0.88 | 2.99 | 6.17 | 1.58 | 2.67 | 0.61 | 173.20 | 169.95 | 156.93 | 153.56 |
| C2 | 0.70 | 2.85 | 5.85 | 1.58 | 2.57 | 0.53 | 208.31 | 145.62 | 152.47 | 152.86 |
| C3 | 0.57 | 2.69 | 5.75 | 1.57 | 2.39 | 0.58 | 218.93 | 156.59 | 149.64 | 134.84 |

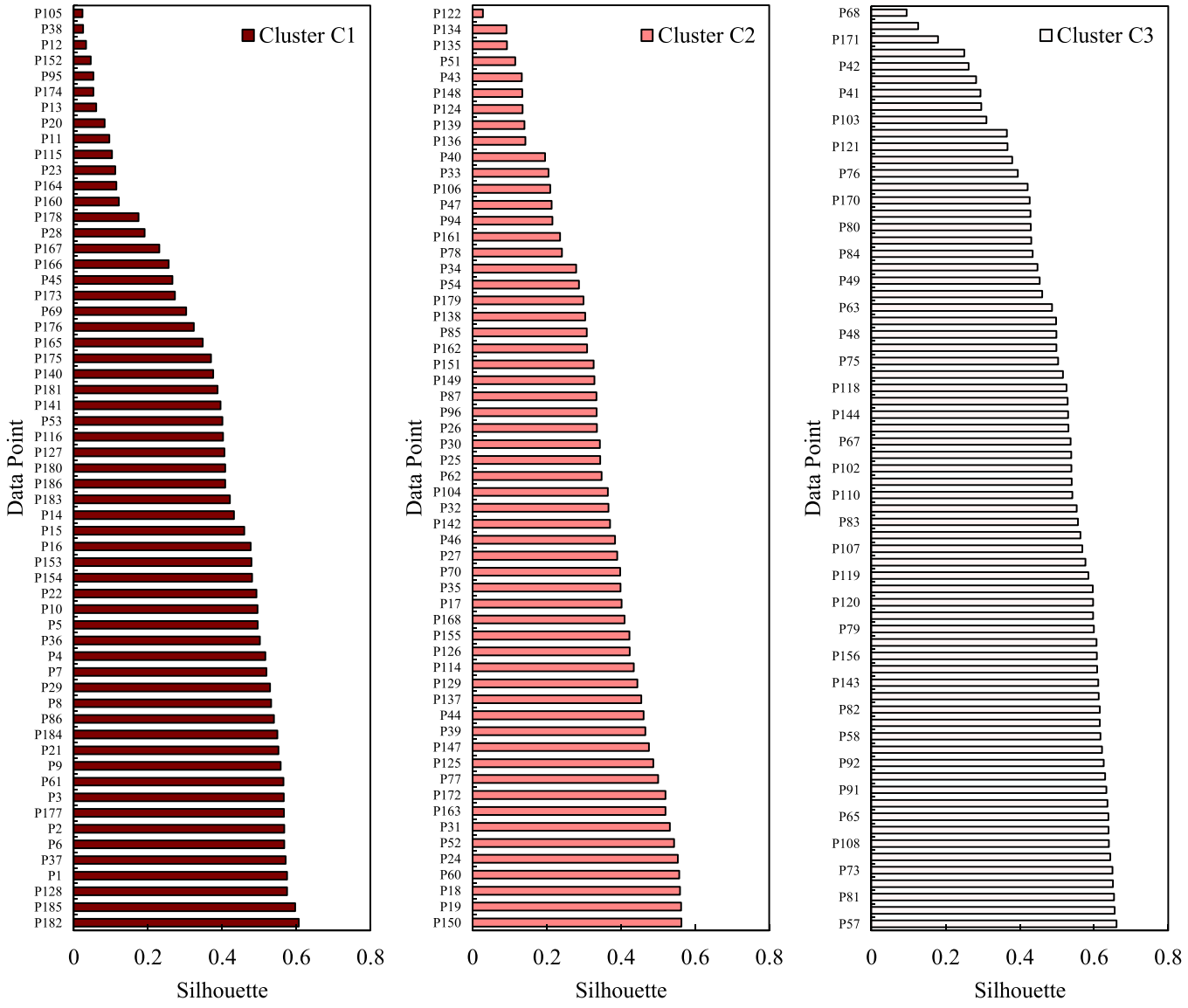


**Fig. 3.** Silhouette scores for the three clusters.

increase in ETo was observed for both extreme scenarios and the MLP-M5P ensemble model. The highest predicted peak value with MLP-M5P was 6.50 mm/day, while RCP 4.5 and RCP 8.5 showed peak ETo values of 6.88 and 6.94 mm/day, respectively. Furthermore, from 2001 to 2041, the mean ETo value on a 10-year scale increased from 3.07 mm/day to 3.18 mm/day for RCP 4.5, with an increase of 3.62%; from 3.05 mm/day to 3.21 mm/day for RCP 8.5, with an increase of 5.32%; and from 3.06 mm/day to 3.20 mm/day for MLP-M5P, with an increase of 4.34%. In addition, from 2041 to 2091, a further increase was observed, with ETo values that reached 3.30 mm/day for RCP 4.5 (an increase of 3.76%), 3.49 mm/day for RCP 8.5 (an increase of 8.85%), and 3.38 mm/day for MLP-M5P (an increase of 6.17%). The overall increases during the forecast period, from 2001 to 2091, were 7.52% for RCP 4.5, 14.64% for RCP 8.5%, and 10.78% for MLP-M5P (Fig. 6c). Thus, the ensemble model resulted in intermediate predicted values between the two extreme scenarios, with RCP 8.5 leading to significantly larger increases in the period 2041–2091 than RCP 4.5. The evaluation metrics (Table 3) also showed high agreement between RCP 4.5 and MLP-M5P ($R^2$ = 0.97, RMSE = 0.28 mm/day, MDA = 99.11%) and RCP 8.5 and MLP-M5P ($R^2$ = 0.97, RMSE = 0.27 mm/day, MDA = 98.40%).

Cluster C2 was characterized by a historical ETo peak of 5.76 mm/day (Fig. 7a), lower than those estimated for Cluster C1, with also a small change in the mean ETo on a 10-year scale from 2.85 mm/day in 1951–2.87 mm/day in 1991, with a low peak in 1961 (as observed for Cluster C1) of 2.79 mm/day (Fig. 7c). The forecast period (Fig. 7b)

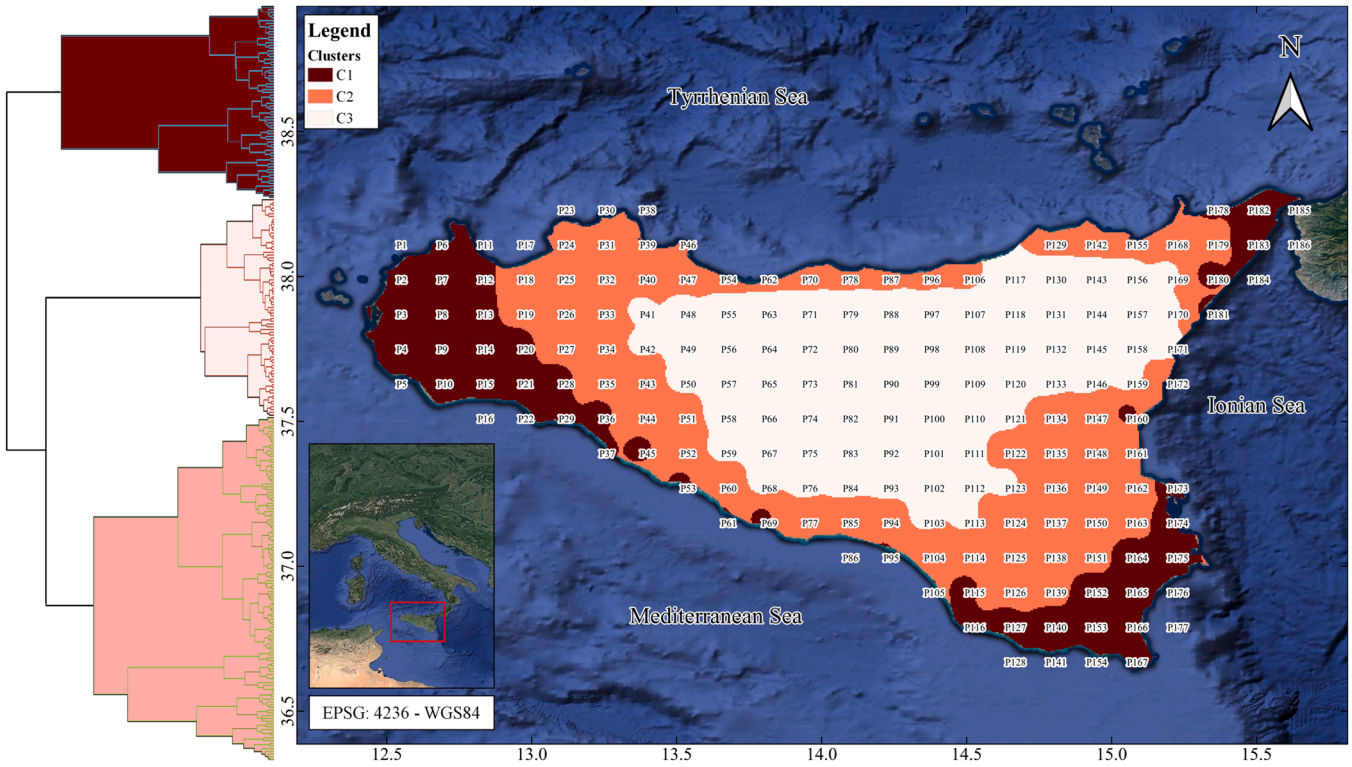


**Fig. 4.** ETo clustering of Sicily, with the dendrogram diagram.

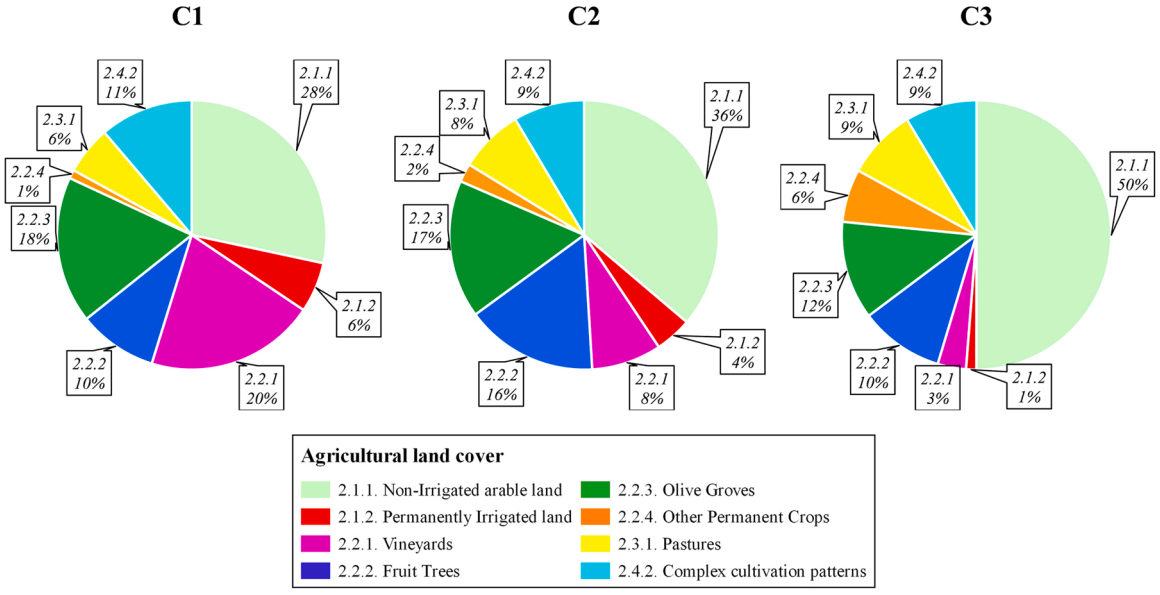


**Fig. 5.** Pie charts of the agricultural land cover for the three clusters.

showed a significant ETo increase with peaks of 6.66 mm/day, 6.67 mm/day, and 6.29 mm/day, for RCP 4.5, RCP 8.5, and MLP-M5P, respectively. Furthermore, the mean ETo on a 10-year scale showed percentage increases of 2.97%, 5.49%, and 5.97% for RCP 4.5, RCP 8.5, and MLP-M5P, respectively, over the period 2001–2041, while for the period 2041–2091, the percentage increases were 4.36%, 9.13%, and 8.30%, respectively. Overall, the increases over the forecast period, between 2001 and 2091, were 7.46%, 15.12%, and 14.77% for RCP 4.5, RCP 8.5, and MLP-M5P, respectively (Fig. 7c). Therefore, the ensemble model resulted in future predictions close to RCP 8.5, which is the most extreme scenario.

The assessment metrics were still high but lower than in cluster C1 with $R^2$ being 0.96 for both RCP 4.5 and MLP-M5P, and RCP 8.5 and MLP-M5P, RMSE between 0.31 mm/day (RCP 4.5 and MLP-M5P) and 0.35 mm/day (RCP 8.5 and MLP-M5P) and an MDA between 97.16% (RCP 4.5 and MLP-M5P) and 97.51% (RCP 8.5 and MLP-M5P).

Cluster C3 showed a lower historical ETo peak compared to C1 and C2, equal to 5.70 mm/day (Fig. 8a). However, significant changes in the mean ETo on a 10-year scale were also assessed. From 1951–1961, a reduction in ETo was estimated from 2.69 mm/day to 2.62 mm/day. The highest peak of 2.72 mm/day, was computed for 1981, with the lowest ETo equal to 2.70 mm/day in 1991 (Fig. 8c).

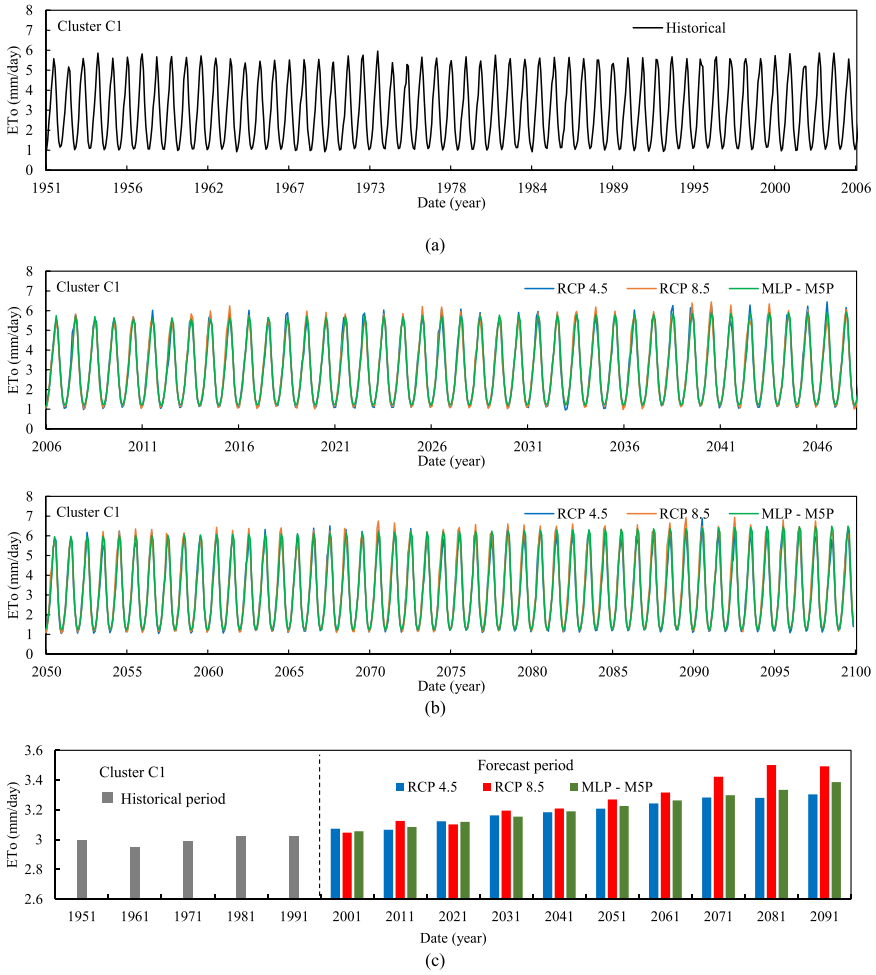


**Fig. 6.** Clusters C1: historical mean ETo (a); predicted mean ETo (b); mean ETo on a ten-year scale (c).

**Table 3**
Evaluation metrics for the different clusters.

| Cluster | Evaluation metrics | RCP 4.5 – MLP-M5P | RCP 8.5 – MLP-M5P |
|---|---|---|---|
| C1 | $R^2$ | 0.97 | 0.97 |
| | RMSE (mm/day) | 0.28 | 0.27 |
| | MAE (mm/day) | 0.19 | 0.20 |
| | MAPE (%) | 5.92 | 6.15 |
| | MDA (%) | 99.11 | 98.40 |
| C2 | $R^2$ | 0.96 | 0.96 |
| | RMSE (mm/day) | 0.31 | 0.35 |
| | MAE (mm/day) | 0.22 | 0.25 |
| | MAPE (%) | 7.58 | 8.14 |
| | MDA (%) | 97.16 | 97.51 |
| C3 | $R^2$ | 0.96 | 0.96 |
| | RMSE (mm/day) | 0.33 | 0.35 |
| | MAE (mm/day) | 0.24 | 0.26 |
| | MAPE (%) | 8.60 | 9.29 |
| | MDA (%) | 96.63 | 96.71 |

However, the forecast period (Fig. 8b) showed an increase in ETo with peaks of 6.56 mm/day (RCP 4.5), 6.60 mm/day (RCP 8.5), and 6.29 mm/day (MLP-M5P). Furthermore, from 2001 to 2041, the 10-year average ETo showed increases of 3.27%, 5.97%, and 6.47% for RCP 4.5, RCP 8.5, and MLP-M5P, respectively, while over the period 2041–2091, the increases were 4.70%, 10.13%, and 7.99%, respectively. Overall, the increases over the entire forecast period, between 2001 and 2091, were 8.12%, 16.71%, and 14.98% for RCP 4.5, RCP 8.5 and MLP-M5P, respectively (Fig. 8c). Thus, C3 showed the lowest ETo values and the highest percentage increases compared to C1 and C2. In addition, as with cluster C2, the ensemble model resulted in ETo predictions and trends closer to RCP 8.5 than RCP 4.5.

The evaluation metrics values were in line with those computed for cluster C2, with $R^2$ being 0.96 for both RCP 4.5 and MLP-M5P, and RCP 8.5 and MLP-M5P, RMSE between 0.33 mm/day (RCP 4.5 and MLP-M5P) and 0.35 mm/day (RCP 8.5 and MLP-M5P) and an MDA between 96.63% (RCP 4.5 and MLP-M5P) and 96.71% (RCP 8.5 and MLP-M5P). Overall, the metrics were in line with a recent literature study. Maqsood et al. (2022), who investigated the future ETo under different RCP climate scenarios for Prince Edward Island (Canada), compared the ETo evaluated with the HS equation with that evaluated with three algorithms, 1D-CNN, LSTM, and MLP, and obtained values of $R^2$ between 0.92 and 0.96 and RMSE between 0.26 and 0.36, comparable to the metrics estimated in this study.

Fig. 9 shows maps of the mean ETo (obtained using the IDW method) for two historical decades: one further back in time, between 1951 and 1960, and one more recent, between 1991 and 2000. In addition, two future decades were also represented for both RCP 4.5 and RCP 8.5 climate scenarios and for the MLP-M5P ensemble model: one for an intermediate time horizon, between 2041 and 2050, and one for the more distant time horizon, between 2091 and 2100. For all decades, in agreement with the previous ETo analysis for the different clusters, the highest and lowest values of ETo were calculated for clusters C1 and C3, respectively.

In the decade 1951–1960, lower average ETo values of 3 mm/day, 2.85 mm/day, and 2.69 mm/day were observed for clusters C1, C2, and C3, respectively. A slight increase was observed in the decade

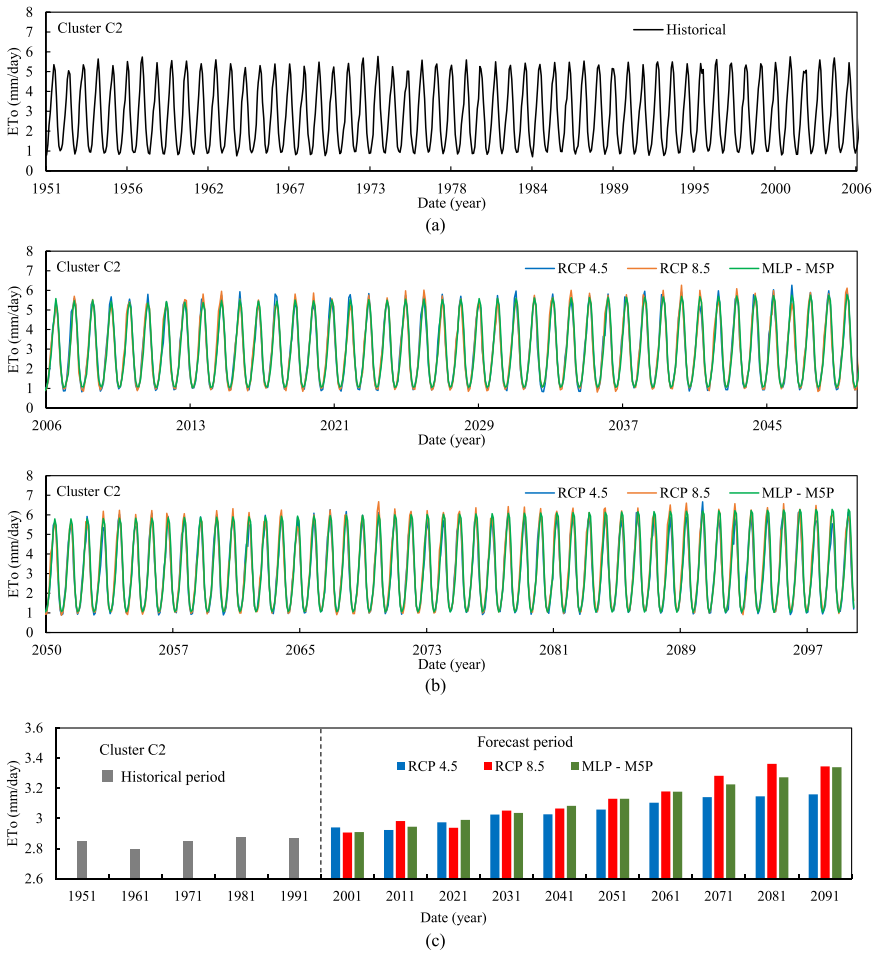


**Fig. 7.** Clusters C2: historical ETo (a); predicted ETo (b); mean ETo on a ten-year scale (c).

1991–2000, with 3.02 mm/day, 2.87 mm/day and 2.71 mm/day for C1, C2 and C3, respectively. However, a significant increase can be observed during the forecast period for both climate scenarios and the ensemble model. The decade 2041–2050 showed average ETo values ranging from 2.97 mm/day (C3) to 3.19 mm/day (C1) for the ensemble model, almost in line with those for RCP 8.5, which range from 2.92 mm/day (C3) to 3.21 mm/day (C1). However, for the last decade, 2091–2100, the RCP 8.5 resulted in ETo values ranging from 3.21 mm/day (C3) to 3.49 mm/day (C1), which were higher than those calculated for the ensemble model, ranging from 3.21 mm/day (C3) to 3.39 mm/day (C1), while RCP 4.5 resulted in lower ETo values, ranging from 3.02 mm/day (C3) to 3.30 mm/day (C1).

### 3.3. ETo analysis for reference data points

An additional insight of this study was to analyze the predictions of the MLP-M5P ensemble model for both high and low silhouette score data points. For this purpose, 6 data points were chosen, 2 for each cluster. Indeed, while a high Silhouette score value indicates a strong belonging to a given subregion of Sicily, a low Silhouette score may represent a borderline situation with ETo trends that may differ from the typical ones observed for each cluster. Figs. 10 and 11 show the average ETo on a 10-year scale for selected data points. Further insight into the comparison between ensemble models and climate scenarios was provided by examining the box plots for the highest and lowest Silhouette data points (Fig. 12), showing the residuals, expressed as the difference between predictions of each model with the others. Each box plot's lower and upper extremes indicate the 1st quartile (25th percentile) and the 3rd quartile (75th percentile), respectively. The whiskers extend from the box bottom to the smallest non-outlier and from the box top to the highest non-outlier.

The 10-year average ETo for the data points with the highest Silhouette score showed an increasing trend for each cluster, with MLP-M5P leading to predicted values between RCP 4.5 and RCP 8.5. However, during the last investigated decades, approximately from 2071 onwards, MLP-M5P led to predictions closer to, but still slightly lower than, RCP 8.5 (Fig. 10). The evaluation metrics for the highest Silhouette data points (Table 4) show a lower agreement between climate scenarios and the ensemble model for data point P182 (cluster C1), with $R^2$ values equal to 0.93 for both RCP 4.5 and MLP-M5P, and RCP 8.5 and MLP-M5P, RMSE between 0.40 mm/day (RCP 4.5 and MLP-M5P) and 0.47 mm/day (RCP 8.5 and MLP-M5P) and an MDA between 90.41% (RCP 8.5 and MLP-M5P) and 90.94% (RCP 4.5 and MLP-M5P). Instead, data points P150 (cluster C2) and P57 (cluster C3) show metrics in line with those computed for their clusters (Table 3) with $R^2$ values between 0.96 (cluster C3, RCP 4.5 and MLP-M5P) and 0.97 (cluster C2, RCP 4.5 and MLP-M5P and RCP 8.5 and MLP-M5P, cluster C3, RCP 8.5 and MLP-M5P). This evidence was also confirmed by the box plots (Fig. 12) that showed relatively higher residuals for cluster C1 compared to clusters C2 and C3. However, boxes showed a narrow and symmetrical shape, ranging from − 0.5 mm/day to 0.5 mm/day with the center close to 0 for all clusters.

For the lowest Silhouette data points, MLP-M5P led to predictions in line with RCP 4.5, with the extreme scenario RCP 8.5 showing far more significant increases than RCP 4.5 and MLP-M5P (Fig. 11). Furthermore, looking at the data points for clusters C2 and C3, the borderline nature of these points can be noted. In particular, point P68 (Cluster C3) showed higher ETo averages during the historical period than those observed for

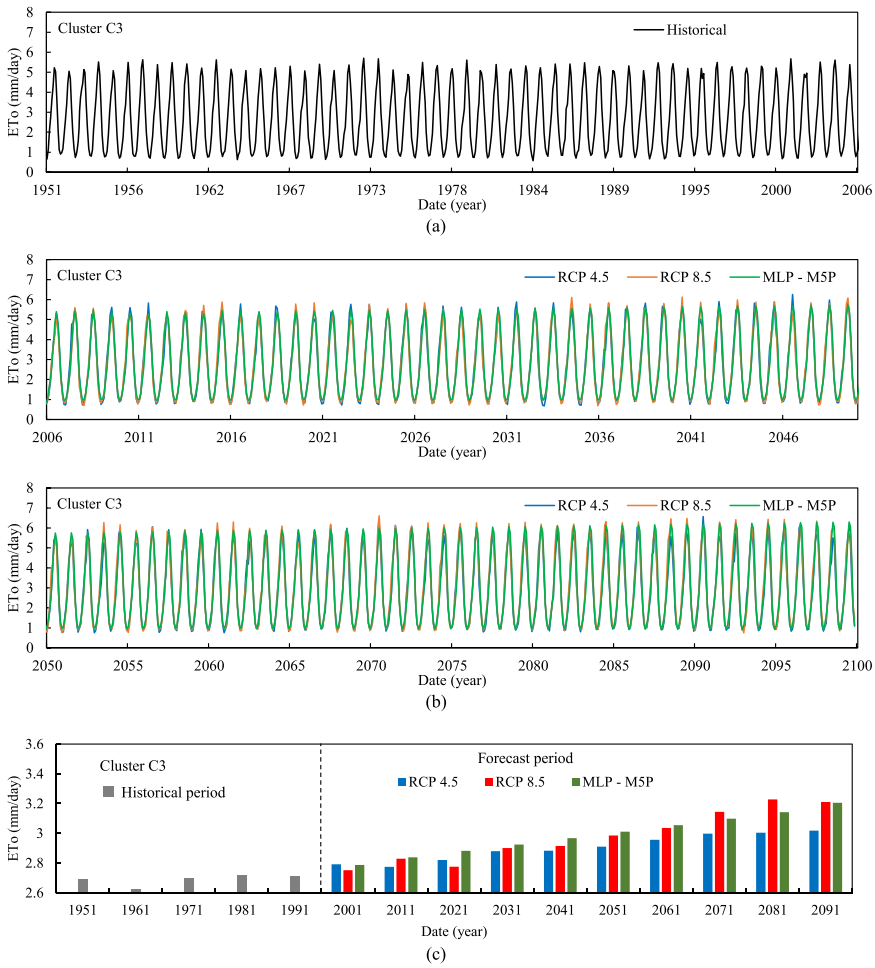


**Fig. 8.** Clusters C3: historical ETo (a); predicted ETo (b); mean ETo on a ten-year scale (c).

point P122 (Cluster C2). This result disagrees with the evidence from clustering analysis and the data points with high Silhouette. This can be explained by the greater proximity to the coastline of point P68 compared to point P122, which led to a higher $ETo_{Mean}$ for P68. However, the other statistical parameters (e.g., $ETo_{0–1.5}$, $ETo_{1.5–3.0}$ $ETo_{3.0–4.5}$ and $ETo_{4.5–6.0}$), confirmed the belonging of points P122 and P68 to clusters C2 and C3, respectively.

Evaluation metrics for the lowest Silhouette score data points (Table 5) showed a high agreement between RCP 4.5, RCP 8.5, and MLP-M5P with $R^2$ values between 0.97 (cluster C1, RCP 8.5 – MLP-M5P, cluster C2, RCP 4.5 – MLP-M5P, cluster C3, RCP 4.5 – MLP-M5P, and cluster C3, RCP 8.5 – MLP-M5P) and 0.98 (cluster C1, RCP 4.5 – MLP-M5P, and cluster C2, RCP 8.5 – MLP-M5P), RMSE between 0.25 mm/day (cluster C1, RCP 8.5 – MLP-M5P) and 0.32 mm/day (cluster C3, RCP 8.5 – MLP-M5P), and MDA between 96.71% (cluster C1, RCP 4.5 – MLP-M5P) and 97.69% (cluster C2, RCP 8.5 – MLP-M5P). The high agreement between climate scenarios and the ensemble model was also confirmed by the box plots that appeared narrower compared to the box plots related to points with high Silhouette scores (Fig. 12).

Overall, the evaluation metrics calculated for low Silhouette data points were in line with or even higher than those calculated for high. On the one hand, this result confirms the tendency of the ensemble model to provide forecasts in line with future scenarios for points characterized by more certain and uncertain inclusion in clusters. On the other hand, a slightly lower ETo difference was observed between the RCP 4.5 and RCP 8.5 future climate scenarios for lower Silhouette data points compared to those with higher Silhouette. This feature is particularly evident when comparing high and low Silhouette data points for cluster C1, for which a marked difference in ETo was observed between RCP 4.5 and RCP 8.5. Consequently, the ensemble model, which led to intermediate scenarios between RCP 4.5 and RCP 8.5, showed slightly worse metrics for high Silhouette data points. However, the differences between low and high Silhouette data points were less marked for Cluster C2 and even less so for Cluster C3, highlighting a lower variability of ETo, with the future climate scenarios, for the inland of Sicily (C3 also showed the lower values of $ETo_{std}$ and $ETo_{skew}$).

Overall, increasing ETo values were observed for both future climate scenarios RCP 4.5 and RCP 8.5 and based on the MLP-M5P model predictions. From this perspective, increasingly careful management of water resources is crucial, in order to avoid severe water deficits especially during the irrigation seasons. Therefore, an accurate prediction of hydrological and agronomic variables will have to be combined with an optimization of the irrigation systems and strategies, which are often obsolete in Southern Italy (Giuliani et al., 2019). Consequently, the promotion of localized irrigation techniques (e.g., micro-irrigation and drip irrigation systems) in the context of the current climate change scenario, together with agricultural reuse strategies of treated wastewater (Aiello et al., 2007; Ventura et al., 2019), could have a great future impact on both actual evapotranspiration and management of surface and groundwater resources (Pool et al., 2021; Vanella et al., 2021).

However, it must be pointed out that this study only focuses on a region with a Mediterranean climate. In order to overcome this limitation, it will be interesting in future studies to test the developed approach for the long-term prediction of reference evapotranspiration in different climates, where larger or smaller variations in evapotranspiration can be observed over the seasons.

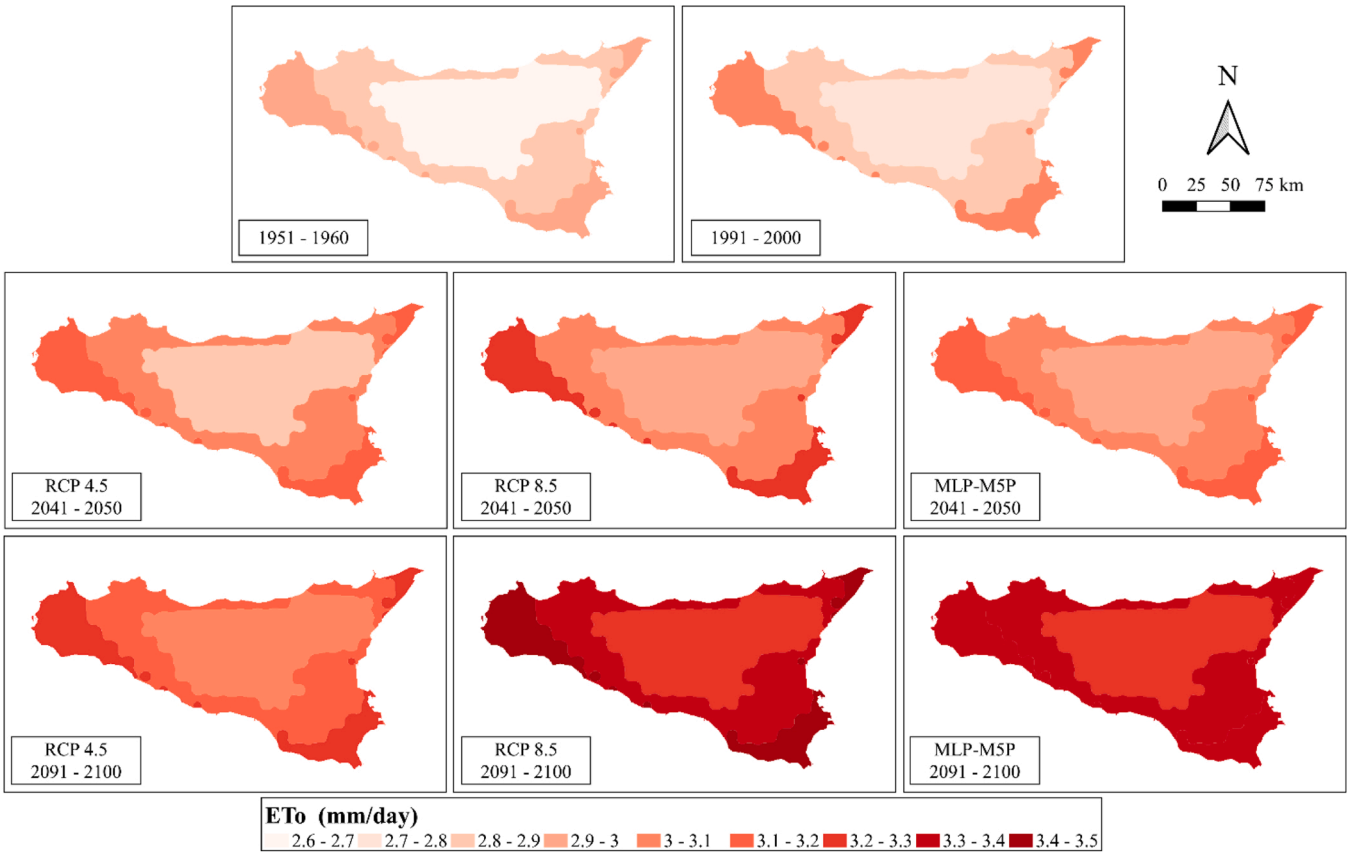


**Fig. 9.** ETo maps of Sicily, periods: 1951–1960; 1991–2000; 2041–2050; 2091–2100.

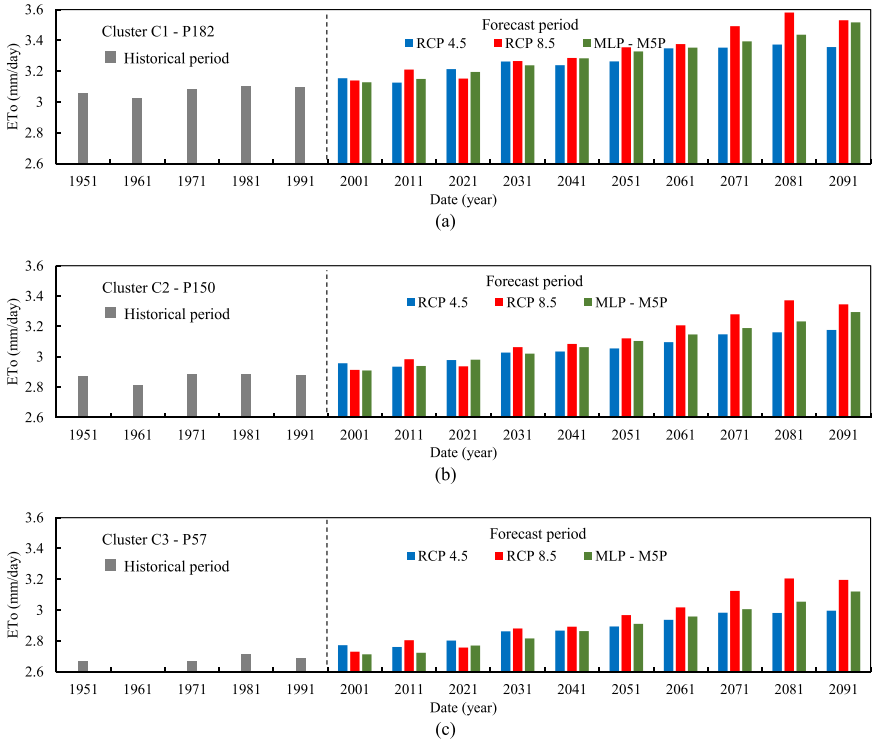


**Fig. 10.** Mean ETo on a ten-year scale for high Silhouette data points, with clusters: C1 (a); C2 (b); C3 (c).

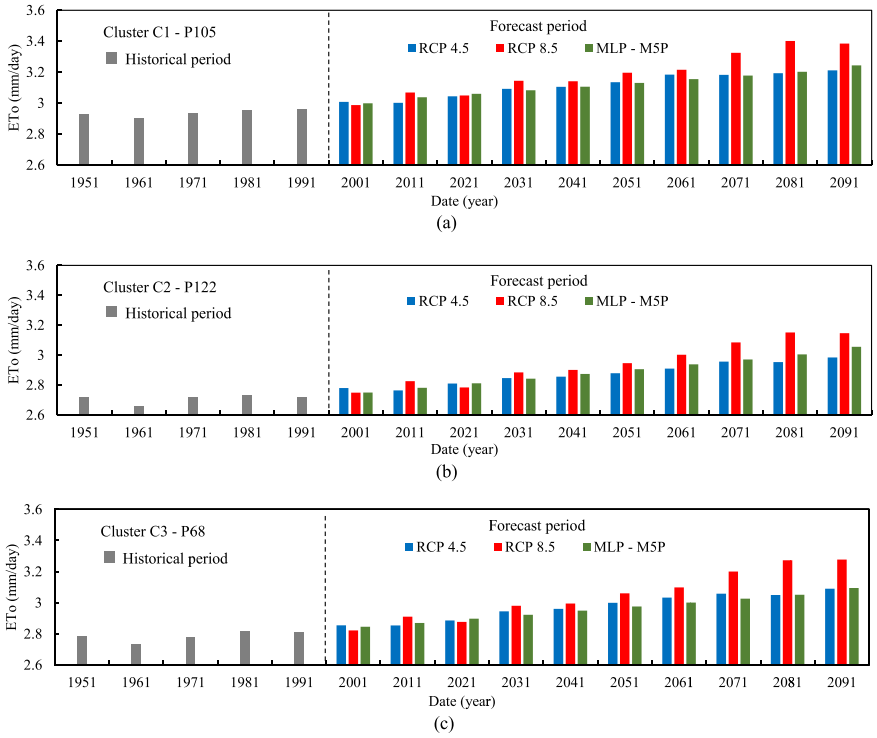


**Fig. 11.** Mean ETo on a ten-year scale for low Silhouette data points, with clusters: C1 (a); C2 (b); C3 (c).

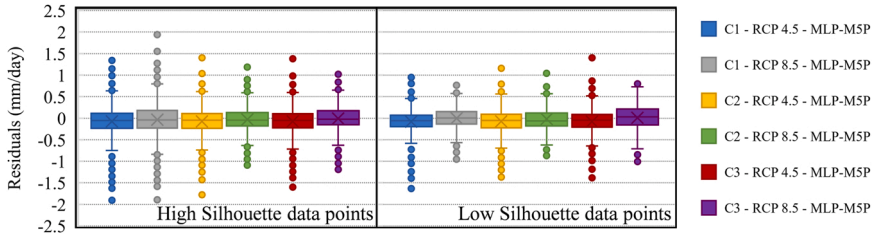


**Fig. 12.** Box plots of residuals for high and low Silhouette data points, with clusters: C1 (a); C2 (b); C3 (c).

**Table 4**
Evaluation metrics for high Silhouette data points.

| Cluster | Evaluation metrics | RCP 4.5 – MLP-M5P | RCP 8.5 – MLP-M5P |
|---|---|---|---|
| C1 | $R^2$ | 0.93 | 0.93 |
| | RMSE (mm/day) | 0.40 | 0.47 |
| | MAE (mm/day) | 0.28 | 0.33 |
| | MAPE (%) | 8.32 | 9.35 |
| | MDA (%) | 90.94 | 90.41 |
| C2 | $R^2$ | 0.97 | 0.97 |
| | RMSE (mm/day) | 0.34 | 0.31 |
| | MAE (mm/day) | 0.24 | 0.23 |
| | MAPE (%) | 8.39 | 8.07 |
| | MDA (%) | 97.34 | 97.34 |
| C3 | $R^2$ | 0.96 | 0.97 |
| | RMSE (mm/day) | 0.34 | 0.33 |
| | MAE (mm/day) | 0.24 | 0.24 |
| | MAPE (%) | 9.06 | 9.06 |
| | MDA (%) | 96.54 | 96.89 |

**Table 5**
Evaluation metrics for low Silhouette data points.

| Cluster | Evaluation metrics | RCP 4.5 – MLP-M5P | RCP 8.5 – MLP-M5P |
|---|---|---|---|
| C1 | $R^2$ | 0.98 | 0.97 |
| | RMSE (mm/day) | 0.30 | 0.25 |
| | MAE (mm/day) | 0.21 | 0.19 |
| | MAPE (%) | 6.69 | 6.33 |
| | MDA (%) | 96.71 | 97.16 |
| C2 | $R^2$ | 0.97 | 0.98 |
| | RMSE (mm/day) | 0.30 | 0.27 |
| | MAE (mm/day) | 0.22 | 0.21 |
| | MAPE (%) | 7.91 | 8.13 |
| | MDA (%) | 97.25 | 97.69 |
| C3 | $R^2$ | 0.97 | 0.97 |
| | RMSE (mm/day) | 0.31 | 0.32 |
| | MAE (mm/day) | 0.22 | 0.25 |
| | MAPE (%) | 8.02 | 9.75 |
| | MDA (%) | 97.07 | 97.07 |

In addition, the combination of the MOHC-HadGEM2-ES, as GCM, and CLMCom-CCLM4–8–17, as RCM, was considered in this study. A comparison with other regional and global climate models could be considered in future research.

A further interesting future application of the implemented methodology could concern the assessment of crop evapotranspiration, taking into account the typical crops with both high and low water demands. This would also help to better highlight similarities and differences in reference and crop evapotranspiration trends for a given area of investigation. From this perspective, different ML or deep-learning algorithms could be included in the forecast procedure in order to improve the reliability of the evapotranspiration prediction. Furthermore,

different clustering algorithms, in addition to the Hierarchical one, could be tested to improve the identification of homogeneous regions based on reference and crop evapotranspiration features.

Finally, although the calibrated Hargreaves-Samani equation has proven to be reliable in the assessment of ETo, for well-instrumented study areas and, more generally, for areas where an appropriate calibration of the empirical Hargreaves coefficient is not available, it might be interesting to test the developed approach to investigate the spatio-temporal variability of the reference evapotranspiration using the Penman-Monteith equation for the ETo evaluation.

## 4. Conclusion

This study provided an extensive spatio-temporal analysis of the evolutionary trends of reference evapotranspiration in Sicily. ETo was first assessed with the Hargreaves-Samani equation, calibrated for the study area, based on historical data and two future climate scenarios: RCP 4.5 and RCP 8.5. The Hierarchical algorithm was used to divide Sicily into three homogeneous regions, each characterized by specific evapotranspiration features. Support Vector Regression was used to forecast $T_{min}$ and $T_{max}$ for the period 2006–2100, while an ensemble model based on MLP and M5P was developed for the ETo prediction in the same period. Then the ETo calculated with the HS equation for the RCP 4.5 and RCP 8.5 future climate scenarios were compared with the forecasting performed with the ensemble MLP-M5P model.

An increasing ETo trend was observed for all three clusters, with the highest values predicted for cluster C1, along the coast, and an overall increase from 2001 to 2091 of 7.52% for RCP 4.5, 14.64% for RCP 8.5%, and 10.78% for MLP-M5P. The lowest values were instead estimated for cluster C3 which, however, was characterized by the highest percentage increases of ETo during the forecast period, amounting to 8.12%, 16.71%, and 14.98% for RCP 4.5, RCP 8.5, and MLP-M5P, respectively. The cluster analysis also showed a higher concentration of agricultural land with higher water demand along the coast, particularly for Cluster C1, which also showed the highest ETo values. This outcome suggests an increased risk of water deficit for the coastal areas of Sicily in the future.

The MLP-M5P ensemble model resulted in future ETo values intermediate between climate scenarios RCP 4.5 and RCP 8.5, with the latter showing the highest values of ETo in all clusters.

Overall, the MLP-M5P ensemble model, trained on the basis of the historical data of both ETo and temperatures, resulted in intermediate trends between RCP 4.5 and RCP 8.5 climate scenarios, proving to be particularly suitable for evapotranspiration predictions in both coastal and inland areas. The developed approach, based on the combination of clustering and forecasting algorithms, provides a concise and reliable assessment of ETo trends, and identifies different homogeneous regions. As the methodology requires a limited number of climate variables, it can be a powerful tool for improving future water resource management planning.

## 5. Declarations

1. The authors have no relevant financial or non-financial interests to disclose.
2. The authors have no competing interests to declare that are relevant to the content of this article.
3. All authors certify that they have no affiliations with or involvement in any organization or entity with any financial interest or non-financial interest in the subject matter or materials discussed in this manuscript.
4. The authors have no financial or proprietary interests in any material discussed in this article.

## Declaration of Competing Interest

The authors declare that they have no known competing financial interests or personal relationships that could have appeared to influence the work reported in this paper.

## Data Availability

Data will be made available on request.

## Appendix A. Supporting information

Supplementary data associated with this article can be found in the online version at doi:10.1016/j.agwat.2023.108232.

## References


Aghelpour, P., Mohammadi, B., Biazar, S.M., 2019. Long-term monthly average temperature forecasting in some climate types of Iran, using the models SARIMA, SVR, and SVR-FA. Theor. Appl. Climatol. 138, 1471–1480. https://doi.org/10.1007/s00704-019-02905-w.

Aiello, R., Cirelli, G.L., Consoli, S., 2007. Effects of reclaimed wastewater irrigation on soil and tomato fruits: a case study in Sicily (Italy). Agric. Water Manag. 93 (1–2), 65–72. https://doi.org/10.1016/j.agwat.2007.06.008.

Aladaileh, H., Al Qinna, M., Karoly, B., Al-Karablieh, E., Rakonczai, J., 2019. An investigation into the spatial and temporal variability of the meteorological drought in Jordan. Climate 7 (6), 82. https://doi.org/10.3390/cli7060082.

Allen, R.G., Pereira, L., Raes, D., Smith, M., 1998. Crop evapotranspiration: guidelines for computing crop water requirements. FAO Irrigation and Drainage Paper 56. Food and Agriculture Organisation, Rome, Italy.

Barton, Y., Giannakaki, P., Von Waldow, H., Chevalier, C., Pfahl, S., Martius, O., 2016. Clustering of regional-scale extreme precipitation events in southern Switzerland. Mon. Weather Rev. 144 (1), 347–369.

Benedetto, G., Giordano, A., 2008. Sicily. In: Vogiatzakis, I.N., Pungetti, G., Mannion, A. M. (Eds.), Mediterranean Island Landscapes. Landscape Series, 9. Springer, Dordrecht. https://doi.org/10.1007/978-1-4020-5064-0_7.

Berhanu, B., Yilma, S., Demisse, S.S., Melesse, A.M., 2015. Flow regime classification and hydrological characterization: a case study of Ethiopian Rivers. Water 7 (6), 3149–3165. https://doi.org/10.3390/w7063149.

Callahan, C., Bridge, H., 2021. Data Mining of Rare Alleles to Assess Biogeographic Ancestry. 2021 Systems and Information Engineering Design Symposium (SIEDS), 1–6, doi: 10.1109/SIEDS52267.2021.9483709.

Chaouche, K., Neppel, L., Dieulin, C., Pujol, N., Ladouche, B., Martin, E., Salas, D., Caballero, Y., 2010. Analyses of precipitation, temperature and evapotranspiration in a French Mediterranean region in the context of climate change. Compted Rendus Geosci. 342 (3), 234–243. https://doi.org/10.1016/j.crte.2010.02.001.

Chen, Z., Zhu, Z., Jiang, H., Sun, S., 2020. Estimating daily reference evapotranspiration based on limited meteorological data using deep learning and classical machine learning methods. J. Hydrol. https://doi.org/10.1016/j.jhydrol.2020.125286.

Chia, M.Y., Huang, Y.F., Koo, C.H., Ng, J.L., Ahmed, A.N., El-Shafie, A., 2022a. Long-term forecasting of monthly mean reference evapotranspiration using deep neural network: a comparison of training strategies and approaches. Appl. Soft Comput. 126, 109221 https://doi.org/10.1016/j.asoc.2022.109221.

Chia, M.Y., Huang, Y.F., Koo, C.H., 2022b. Resolving data-hungry nature of machine learning reference evapotranspiration estimating models using inter-model ensembles with various data management schemes. Agric. Water Manag. 261, 107343 https://doi.org/10.1016/j.agwat.2021.107343.

CLMCom, 2017. CORDEX EUR-44 CLMcom CCLM4–8-17. World Data Center for Climate (WDCC) at DKRZ. ⟨http://cera-www.dkrz.de/WDCC/ui/Compact.jsp?acronym=CXEU44CLCL⟩.

Cortes, C., Vapnik, V., 1995. Support-vector networks. Mach. Learn. 20 (3), 273–297.

Dash, M., Koot, P., 2009. Feature selection for clustering. In: Liu, L., Özsu, M.T. (Eds.), Encyclopedia of Database Systems. Springer, US, pp. 1119–1125.

Di Nunno, F., Granata, F., 2020. Groundwater level prediction in Apulia region (Southern Italy) using NARX neural network. Environ. Res. 190, 110062 https://doi.org/10.1016/j.envres.2020.110062.

Di Nunno, F., Granata, F., Pham, Q.B., de Marinis, G., 2022. Precipitation forecasting in Northern Bangladesh using a hybrid machine learning model. Sustainability 14 (5), 2663. https://doi.org/10.3390/su14052663.

Dosio, A., 2016. Projections of climate change indices of temperature and precipitation from an ensemble of bias-adjusted high-resolution EURO-CORDEX regional climate models. J. Geophys. Res. Atmos. 121 (10), 5488–5511. https://doi.org/10.1002/2015JD024411.

Elbeltagi, A., Deng, J., Wang, K., Malik, A., Maroufpoor, S., 2020. Modeling long-term dynamics of crop evapotranspiration using deep learning in a semi-arid environment. Agric. Water Manag. 241, 106334 https://doi.org/10.1016/j.agwat.2020.106334.

Eyring, V., Bony, S., Meehl, G.A., Senior, C.A., Stevens, B., Stouffer, R.J., Taylor, K.E., 2016. Overview of the coupled model intercomparison project phase 6 (CMIP6) experimental design and organization. Geosci. Model Dev. 9, 1937–1958. https://doi.org/10.5194/gmd-9-1937-2016, 2016.

Fan, J., Wu, L., Zhang, F., Xiang, Y., Zheng, J., 2016. Climate change effects on reference crop evapotranspiration across different climatic zones of China during 1956–2015. J. Hydrol. 542, 923–937. https://doi.org/10.1016/j.jhydrol.2016.09.060.

Forestieri, A., Lo Conti, F., Blenkinsop, S., Cannarozzo, M., Fowler, H.J., Noto, L., 2018a. Regional frequency analysis of extreme precipitation for Sicily (Italy). Int. J. Climatol. https://doi.org/10.1002/joc.5400.
Forestieri, A., Arnone, E., Blenkinsop, S., Candela, A., Fowler, H., Noto, L.V., 2018b. The impact of climate change on extreme precipitation in Sicily, Italy. Hydrology 32, 332–348. https://doi.org/10.1002/hyp.11421.
Fu, J., Gong, Y., Zheng, W., Zou, J., Zhang, M., Zhang, Z., Qin, J., Liu, J., Quan, B., 2022. Spatial-temporal variations of terrestrial evapotranspiration across China from 2000 to 2019. Sci. Total Environ. 825, 153951 https://doi.org/10.1016/j.scitotenv.2022.153951.
Giuliani, M.M., Gatta, G., Cappelli, G., et al., 2019. Identifying the most promising agronomic adaptation strategies for the tomato growing systems in Southern Italy via simulation modeling. Eur. J. Agron. 111, 125937 https://doi.org/10.1016/j.eja.2019.125937.
Goyal, R.K., Gaur, M.K., 2022. The implications of climate change on water resources of Rajasthan. In: Goyal, M.K., Gupta, A.K., Gupta, A. (Eds.), Hydro-Meteorological Extremes and Disasters. Disaster Resilience and Green Growth. Springer, Singapore. https://doi.org/10.1007/978-981-19-0725-8_15.
Granata, F., Di Nunno, F., 2021a. Forecasting evapotranspiration in different climates using ensembles of recurrent neural networks. Agric. Water Manag. 255, 107040 https://doi.org/10.1016/j.agwat.2021.107040.
Granata, F., Di Nunno, F., 2021b. Artificial Intelligence models for prediction of the tide level in Venice. Stoch. Environ. Res. Risk Assess. 35, 2537–2548. https://doi.org/10.1007/s00477-021-02018-9.
Gutowski, W., Giorgi, F., Timbal, B., Frigon, A., Jacob, D., Kang, H., Raghavan, K., Lee, B., Lennard, C., Nikulin, G., Rourke, E.O., Rixen, M., 2016. WCRP coordinated regional downscaling EXperiment (CORDEX): a diagnostic MIP for CMIP6. Geosci. Model Dev. Discuss. 9, 4087–4095. https://doi.org/10.5194/gmd-9-4087-2016.
Hargreaves, G., Samani, Z., 1985. Reference crop evapotranspiration from temperature. Appl. Eng. Agric. 1 (2), 96–99. https://doi.org/10.13031/2013.26773.
Hobeichi, S., Abramowitz, G., Evans, J.P., 2021. Robust historical evapotranspiration trends across climate regimes. Hydrol. Earth Syst. Sci. 25 (7), 3855–3874. https://doi.org/10.5194/hess-25-3855-2021.
Höök, M., Sivertsson, A., Aleklett, K., 2010. Validity of the fossil fuel production outlooks in the IPCC emission scenarios. Nat. Resour. Res. 19 (2), 63–81. https://doi.org/10.1007/s11053-010-9113-1.
Jerin, J.N., Islam, H.M.T., Islam, A.R.M.T., Shahid, S., Hu, Z., Badhan, M.A., Chu, R., Elbeltagi, A., 2021. Spatiotemporal trends in reference evapotranspiration and its driving factors in Bangladesh. Theor. Appl. Climatol. 144, 793–808. https://doi.org/10.1007/s00704-021-03566-4.
Kadkhodazadeh, M., Valikhan Anaraki, M., Morshed-Bozorgdel, A., Farzin, S., 2022. A new methodology for reference evapotranspiration prediction and uncertainty analysis under climate change conditions based on machine learning, multi criteria decision making and Monte Carlo Methods. Sustainability 14 (5), 2601. https://doi.org/10.3390/su14052601.
Karbasi, M., Jamei, M., Ali, M., Malik, A., Yaseen, Z.M., 2022. orecasting weekly reference evapotranspiration using auto encoder decoder bidirectional LSTM model hybridized with a Boruta-CatBoost input optimizer. Comput. Electron. Agric. 198, 107121 https://doi.org/10.1016/j.compag.2022.107121.
Li, Y., Yao, N., Chau, H.W., 2017. Influences of removing linear and nonlinear trends from climatic variables on temporal variations of annual reference crop evapotranspiration in Xinjiang, China. Sci. Total Environ. 592, 680–692. https://doi.org/10.1016/j.scitotenv.2017.02.196.
Li, Y., Liang, Z., Hu, Y., Li, B., Xu, B., Wang, D., 2020. A multi-model integration method for monthly streamflow prediction: modified stacking ensemble strategy. J. Hydroinformatics 22 (2), 310–326. https://doi.org/10.2166/hydro.2019.066.
Liuzzo, L., Noto, L.V., Arnone, E., Caracciolo, D., La Loggia, G., 2015. Modifications in water resources availability under climate changes: a case study in a Sicilian Basin. Water Resour. Manag. 29, 1117–1135. https://doi.org/10.1007/s11269-014-0864-z.
Malik, A., Jamei, M., Ali, M., Prasad, R., Karbasi, M., Yaseen, Z.M., 2022. Multi-step daily forecasting of reference evapotranspiration for different climates of India: a modern multivariate complementary technique reinforced with ridge regression feature selection. Agric. Water Manag. 272, 107812 https://doi.org/10.1016/j.agwat.2022.107812.
Markantonis, I., Vlachogiannis, D., Sfetsos, A., Kioutsioukis, I., 2022. Extreme wet-cold compound events investigation under climate change in Greece, EGUsphere [preprint], doi: 10.5194/egusphere-2022–48.
Masanta, S.K., Vemavarapu, S.V., 2020. Regionalization of evapotranspiration using fuzzy dynamic clustering approach. Part 1: Formation of regions in India. Int. J. Climatol. 40, 3514–3530. https://doi.org/10.1002/joc.6411.
Mendicino, G., Senatore, A., 2013. Regionalization of the hargreaves coefficient for the assessment of distributed reference evapotranspiration in Southern Italy. J. Irrig. Drain. Eng. 139 (5), 349–362. https://doi.org/10.1061/(ASCE)IR.1943-4774.0000547.
Murtagh, F., 1991. Multilayer perceptrons for classification and regression. Neurocomputing 2 (5–6), 183–197.
Neto, R.M.B., Santos, C.A.G., da Silva, R.M., dos Santos, C.A.C., Liu, Z., Quinn, N.W., 2021. Geospatial cluster analysis of the state, duration and severity of drought over Paraíba State, northeastern Brazil. Sci. Total Environ. 799, 149492 https://doi.org/10.1016/j.scitotenv.2021.149492.
Pandey, B.K., Khare, D., 2018. Identification of trend in long term precipitation and reference evapotranspiration over Narmada River basin (India). Glob. Planet. Change 161, 172–182. https://doi.org/10.1016/j.gloplacha.2017.12.017.
Peres, D.J., Senatore, A., Nanni, P., Cancelliere, A., Mendicino, G., Bonaccorso, B., 2020. Evaluation of EURO-CORDEX (Coordinated Regional Climate Downscaling Experiment for the Euro-Mediterranean area) historical simulations by high-quality observational datasets in southern Italy: insights on drought assessment. Nat. Hazard. Earth Syst. Sci. 20, 3057–3082. https://doi.org/10.5194/nhess-20-3057-2020, 2020.
Pham, Q.B., Kumar, M., Di Nunno, F., Elbeltagi, A., Granata, F., Islam, A.R.M.T., Talukdar, S., Nguyen, X.C., Ahmed, A.N., Anh, D.T., 2022. Groundwater level prediction using machine learning algorithms in a drought-prone area. Neural Comput. Appl. https://doi.org/10.1007/s00521-022-07009-7.
Piani, C., Haerter, J.O., Coppola, E., 2010. Statistical bias correction for daily precipitation in regional climate models over Europe. Theor. Appl. Climatol. 99 (1–2), 187–192. https://doi.org/10.1007/s00704-009-0134-9.
Pool, S., Francés, F., Garcia-Prats, A., Pulido-Velazquez, M., et al., 2021. From flood to drip irrigation under climate change: Impacts on evapotranspiration and groundwater recharge in the Mediterranean region of Valencia (Spain). e2020EF001859 Earth's Future 9. https://doi.org/10.1029/2020EF001859.
Prăvălie, R., Piticar, A., Roşca, B., Sfică, L., Bandoc, G., Tiscovschi, A., Patrich, C., 2019. Spatio-temporal changes of the climatic water balance in Romania as a response to precipitation and reference evapotranspiration trends during 1961–2013. CATENA 172, 295–312. https://doi.org/10.1016/j.catena.2018.08.028.
Quinlan, J.R., 1992. Learning with continuous classes. In 5th Australian Joint Conference on Artificial Intelligence, Hobart, Australia, 16–18 November 1992; World Scientific: Singapore 1992, 343–348.
Regione Sicilia, 2010. Piano di gestione del distretto idrografico della Sicilia. In Italian.
Rosenblatt, F. 1961. Principles of neurodynamics. perceptrons and the theory of brain mechanisms. Cornell Aeronautical Lab Inc Buffalo NY.
Rousseeuw, P.J., 1987. Silhouettes: a graphical aid to the interpretation and validation of cluster analysis. Comput. Appl. 20, 53–65. https://doi.org/10.1016/0377-0427(87)90125-7.
She, D., Xia, J., Zhang, Y., 2017. Changes in reference evapotranspiration and its driving factors in the middle reaches of Yellow River Basin, China. Sci. Total Environ. 607–608, 1151–1162. https://doi.org/10.1016/j.scitotenv.2017.07.007.
Shutaywi, M., Kachouie, N.N., 2021. Silhouette analysis for performance evaluation in machine learning with applications to clustering. Entropy 23 (6), 759. https://doi.org/10.3390/e23060759.
The HadGEM2 Development Team, 2011. The HadGEM2 family of Met Office Unified Model climate configurations. Geosci. Model Dev. 4, 723–757. https://doi.org/10.5194/gmd-4-723-2011, 2011.
Tikhamarine, Y., Malik, A., Kumar, A., Souag-Gamane, D., Kisi, O., 2019. Estimation of monthly reference evapotranspiration using novel hybrid machine learning approaches. Hydrol. Sci. J. 64 (15), 1824–1842. https://doi.org/10.1080/02626667.2019.1678750.
Tikhamarine, Y., Malik, A., Pandey, K., Sammen, S.S., Souag-Gamane, D., Heddam, S., Kisi, O., 2020a. Monthly evapotranspiration estimation using optimal climatic parameters: efficacy of hybrid support vector regression integrated with whale optimization algorithm. Environ. Monit. Assess. 192, 696. https://doi.org/10.1007/s10661-020-08659-7.
Tikhamarine, Y., Malik, A., Souag-Gamane, D., Kisi, O., 2020b. Artificial intelligence models versus empirical equations for modeling monthly reference evapotranspiration. Environ. Sci. Pollut. Res. 27, 30001–30019. https://doi.org/10.1007/s11356-020-08792-3.
Topçu, E., Seçkin, N., Haktanır, N.A., 2022. Drought analyses of Eastern Mediterranean, Seyhan, Ceyhan, and Asi Basins by using aggregate drought index (ADI). Theor. Appl. Climatol. 147, 909–924. https://doi.org/10.1007/s00704-021-03873-w.
Vanella, D., Ferlito, F., Torrisi, B., et al., 2021. Long-term monitoring of deficit irrigation regimes on citrus orchards in Sicily. J. Agric. Eng. 52 (4) https://doi.org/10.4081/jae.2021.1193.
Vapnik, V., 1998. Statistical Learning Theory. Wiley, New-York.
Ventura, D., Consoli, S., Barbagallo, S., et al., 2019. How to overcome barriers for wastewater agricultural reuse in sicily (Italy). Water 11 (2), 335. https://doi.org/10.3390/w11020335.
Viola, F., Liuzzo, L., Noto, L.V., Lo Conti, F., La Loggia, G., 2014. Spatial distribution of temperature trends in Sicily. Int. J. Climatol. 34, 1–17. https://doi.org/10.1002/joc.3657.
Viola, F., Francipane, A., Caracciolo, D., Pumo, D., La Loggia, G., Noto, L.V., 2016. Co-evolution of hydrological components under climate change scenarios in the Mediterranean area. Sci. Total Environ. 544, 515–524. https://doi.org/10.1016/j.scitotenv.2015.12.004.
Wu, J., Chen, X.Y., Zhang, H., Xiong, L.D., Lei, H., Deng, S.H., 2019. Hyperparameter optimization for machine learning models based on Bayesian optimization. J. Electron. Sci. Technol. 17 (1), 26–40. https://doi.org/10.11989/JEST.1674-862X.80904120.
Xing, W., Wang, W., Shao, Q., Yu, Z., Yang, T., Fu, J., 2016. Periodic fluctuation of reference evapotranspiration during the past five decades: does evaporation paradox really exist in China. Sci. Rep. 6, 39503. https://doi.org/10.1038/srep39503.
Xu, S., Yu, Z., Yang, C., Ji, X., Zhang, K., 2018. Trends in evapotranspiration and their responses to climate change and vegetation greening over the upper reaches of the Yellow River Basin. Agric. Meteorol. 263, 118–129. https://doi.org/10.1016/j.agrformet.2018.08.010.
Xulu, S., Peerbhay, K., Gebreslasie, M., Ismail, R., 2019. Unsupervised clustering of forest response to drought stress in Zululand Region, South Africa. Forests 10 (7), 531. https://doi.org/10.3390/f10070531.
Yang, L., Feng, Q., Adamowski, J.F., Yin, Z., Wen, X., Wu, M., Jia, B., Hao, Q., 2020. Spatio-temporal variation of reference evapotranspiration in northwest China based on CORDEX-EA. Atmos. Res. 238, 10486. https://doi.org/10.1016/j.atmosres.2020.104868.

Yin, Z., Feng, Q., Yang, L., Deo, R.C., Wen, X., Si, J., Xiao, S., 2017. Future projection with an extreme-learning machine and support vector regression of reference evapotranspiration in a mountainous inland watershed in North-West China. Water 9 (11), 880. https://doi.org/10.3390/w9110880.

Zotarelli, L., Dukes, M.D., Romero, C.C., Migliaccio, K.W., Morgan, K.T., 2013. Step by Step Calculation of the Penman-Monteith Evapotranspiration (FAO-56 Method). U.S. Department of Agriculture, UF/IFAS Extension Service, University of Florida.

Zou, H., Hastie, T., 2005. Regularization and variable selection via the elastic net. Journal of the Royal Statistical Society. J. R. Stat. Soc. Ser. B Stat. Methodol. 67 (2), 301–320.